FRONT MATTER

Title

- Low-intensity focused ultrasound enables temporal modulation of human midbrain organoid differentiation
- Ultrasound modulates organoid differentiation timing

Authors

Jinseong Jeong[1,†], Yehhyun Jo[1,†], Youngsun Lee[2,3,†], Eunyoung Jang[1], Yeonji Jeong[4], Won Do Heo[4], Jennifer H. Shin[5,6,7], Mi-Ok Lee[2,3,], and Hyunjoo J. Lee[1,8,9,*]*

Affiliations

[1]School of Electrical Engineering, Korea Advanced Institute of Science and Technology (KAIST), Daejeon 34141, Republic of Korea

[2]Stem Cell Convergence Research Center, Korea Research Institute of Bioscience and Biotechnology (KRIBB), Daejeon 34141, Republic of Korea

[3]Department of Bioscience, Korea University of Science and Technology (UST), Daejeon 34113, Republic of Korea

[4]Department of Biological Sciences, Korea Advanced Institute of Science and Technology (KAIST), Daejeon 34141, Republic of Korea.

[5]Department of Mechanical Engineering, Korea Advanced Institute of Science and Technology (KAIST), Daejeon 34141, Republic of Korea

[6]Graduate School of Stem Cell and Regenerative Biology, Korea Advanced Institute of Science and Technology (KAIST), Daejeon 34141, Republic of Korea

[7]KI for Health Science and Technology, Korea Advanced Institute of Science and Technology (KAIST), Daejeon 34141, Republic of Korea

[8]Department of Bio and Brain Engineering, Korea Advanced Institute of Science and Technology (KAIST), Daejeon 34141, Republic of Korea

[9]KAIST Institute for Nano Century (KINC), Daejeon 34141, Republic of Korea

**Corresponding author: Tel.: +82-42-350-7436; E-mail address: hyunjoo.lee@kaist.ac.kr*

Tel.: +82-42-879-8475; E-mail address: molee@kribb.re.kr

[†]These authors contributed equally.

Abstract

Controlling the precise timing of biosignaling cues in complex 3D models such as organoids is critical for guiding cellular differentiation and functional maturation. Ultrasound stimulation, a next-generation neuromodulation modality, offers unique advantages due to its wide range of tunable waveform parameters, including pulse repetition frequency (PRF) and acoustic intensity (I). However, there is still a lack of precision stimulation platforms and comprehensive biomarker assays for selective control of organoid development. Here, we introduce a modular piezoelectric ultrasound stimulation platform that integrates seamlessly with conventional multi-well plates, enabling parameter-controlled neuromodulation of midbrain organoids (mBOs). Using two distinct ultrasound regimes, we demonstrate that ultrasound can specifically modulate cellular differentiation by promoting dopaminergic progenitor markers

while delaying terminal differentiation. Importantly, ultrasound stimulation did not induce cellular damage, as confirmed by the absence of apoptosis and DNA damage markers. This work demonstrates the potential of focused ultrasound as a safe, non-invasive, and tunable biophysical cue for temporal regulation of organoid differentiation and maturation.

Teaser

Temporal modulation of early-stage midbrain organoid differentiation using precision ultrasound stimulation

MAIN TEXT

Introduction

Human pluripotent stem cell (hPSC)-derived organoids recapitulate the complexity of organs and organ systems, which have enabled critical advancements in developmental studies, drug screening, and direct therapeutic interventions (*1-7*). The developmental process of these stem cells requires highly specific signaling factors at precise temporal intervals to guide the differentiation and maturation pathways (*8-11*). Among the early cell types during differentiation, progenitor cells act as a partially specified precursor to a fully differentiated cell type. This intermediate state allows progenitor cells to retain certain cellular characteristics of stem cells with partially determined fates, which is highly beneficial for critical therapeutic applications such as cell transplantation and tissue grafting that require semi-differentiated cells for highly successful integration with the host (*12-14*). To this end, major advances in biochemical and biophysical signaling techniques, such as bioreactor integration, air-liquid interface cultures, and 3D scaffolding, have contributed to the precise temporal control of progenitor cell differentiation (*1, 15-20*).

While a biochemical approach forms the basis for organoid development, there is a need for supplementary interventions to overcome the existing challenges of remotely manipulating the differentiation of progenitor cells in functional organoids with high spatiotemporal resolution (*8, 10, 21, 22*). Direct stimulation modalities such as electrical current, optogenetics, and ultrasound have been used extensively for *in vivo* and *in vitro* neural activation, neuroplasticity modulation, neurogenesis, neuronal differentiation, and cell signaling control (*23-33*). These techniques have been used in conjunction with conventional biological systems to enable a level of precision not possible with unimodal approaches. Among the direct stimulation modalities, low-intensity focused ultrasound (LIFU) is particularly attractive due to its noninvasiveness, reversible neuronal response, high spatiotemporal resolution, and non-genetic modification (*34-46*). There have been a few studies exploring the effects of ultrasound neuromodulation on cortical organoids; however, these studies have not investigated the ultrasound waveform protocol for precise temporal manipulation and are limited in the functional evaluation of various RNA and protein markers of the organoids (*47, 48*). Moreover, studies on functional organoids that recapitulate distinct brain regions, such as midbrain organoids (mBOs), are necessary due to their association with specific neurological disorders. Investigations into the effect of ultrasound stimulation on cellular functionality, such as neurotransmitter secretion, should be accompanied by the effects on cellular differentiation. Thus, there is a need for the development and deployment of precision ultrasound stimulation platforms with comprehensive biomarker analysis for organoids. We hypothesize that critical ultrasound parameters such as pulse repetition frequency (PRF), acoustic intensity, and stimulation duration are able to biophysically modulate the differentiation timing and dopaminergic function of free-floating mBOs.

In this work, we developed a piezoelectric-based ultrasound transducer platform on a modular printed circuit board (PCB) for robust multi-well stimulation of mBOs. Using this

system, we successfully verified acute and chronic neuronal activation of the mBOs over 55 days without cellular damage. Then, we investigated the effects of ultrasound across two key parameters: acoustic intensity and pulse-repetition frequency (PRF). Intensity is a well-established factor for stimulation success, and PRF has elaborated cell-specific and brain region-specific targeting (*30, 49-56*). Our results demonstrate that intensity and PRF are critical for the selective control of the differentiation and function of mBOs. In particular, ultrasound stimulation delivered at a PRF of 3 kHz and intensity of 500 mW/cm^2 promoted the selective differentiation of dopaminergic progenitor cells without inducing cellular damage. This precise modulation was achieved without altering the overall development of other cell types in the midbrain organoids. Our approach supports the utility of ultrasound as a potential mechanical cue for regulating the temporal differentiation and function of midbrain organoids.

Results

Development of the ultrasound platform and stimulation protocol.

We designed a modular and robust platform capable of multi-well stimulation for various conventional well plates. We packaged the PUT in a modular platform with a robust encapsulation layer that doubled as an acoustic coupling medium. To accommodate various configurations of well plate shapes and sizes, we designed our system to be modular by fabricating the single-element PUTs on individual printed circuit boards (PCBs) and using a multi-connector board to drive multiple devices simultaneously. This design enabled multi-well stimulation while maintaining the flexibility to configure the devices as single-element units. (Fig. 1A, Fig. S1, Methods).

To demonstrate the differential effects of ultrasound waveform parameters on biological response, we selected two key parameters, acoustic intensity and PRF, which are critical for stimulation success and cell specificity (*30, 51, 53-56*). All other parameters, such as fundamental frequency (160 kHz), duty cycle (50%), and pulse train duration (10 minutes every two days), were fixed. Our stimulation condition 1 (US1) delivered a spatial-peak pulse average intensity (I_{SPPA}) of 500 mW/cm^2 at a PRF of 3 kHz, while condition 2 (US2) generated an I_{SPPA} of 50 mW/cm^2 at a PRF of 30 Hz (Fig. 1B). Based on previously reported results, we hypothesized that US1 would effectively stimulate and upregulate neuronal processes of the mBOs while US2 would induce a similar but weaker response (*51*). Based on these two distinct modulatory mechanisms, we identified an optimal approach for temporally manipulating dopaminergic progenitor differentiation in mBOs. A control condition with no stimulation was used to measure the effects of ultrasound stimulation.

The midbrain organoids were generated according to the protocol described in the Methods section (Fig. 1C, Methods). hESCs were seeded in ultra-low attachment 96-well plates to facilitate embryoid body formation, and differentiation was initiated by transitioning to N2 medium with SB431542, Noggin, CHIR99021, and SHH. This induction medium was refreshed on days 2, 4, and 6. On day 8, cells were cultured in N2 medium containing FGF8, followed by a switch to B27-based medium on day 11, which was enriched with FGF8, BDNF, and ascorbic acid. From day 14 onward, the organoids were maintained in maturation medium containing BDNF, GDNF, ascorbic acid, db-cAMP, and DAPT, with regular medium changes. Ultrasound stimulation was initiated at maturation day 1 (MD1) and continued every other day until MD55. Organoids were harvested on maturation day 35 (MD35) and maturation day 55 (MD55). ICC, RT-PCR, and ELISA were conducted for MD35 and MD55 organoids (Methods).

For *in vitro* applications using ultrasound stimulation, it is crucial to produce a beam that uniformly encloses the entire biological sample. A full-width half maximum (FWHM) beam size of 2 mm (lateral) by 1 mm (axial) was required to uniformly envelope the mBOs at the bottom of the well plate. To achieve the desired size and location of the ultrasound beam, we considered the resonance modes in the lead zirconate titanate (PZT) disk and the size of the well plates. There

are two different resonance modes in the PZT disk: thickness mode and radial mode (Fig. 1D). Considering that most PZT disks feature a thin and wide cylindrical geometry (*i.e.*, a small thickness and a large diameter), the radial resonance mode frequency is lower than the thickness resonance mode frequency. These geometries indicate that the operation of the PZT disk in radial mode generates a large lateral FWHM beam right in front of the PZT disk surface due to its low frequency. Using finite element method (FEM) simulations, we confirmed that the radial mode beam profile at 160 kHz had a lateral FWHM of 3.6 mm and an axial FWHM of 2.6 mm. In contrast, the thickness mode operation at 1 MHz had a lateral FWHM of 0.3 mm and an axial FWHM of 2.1 mm (Fig. 1E, F). Therefore, to generate a wide beam, radial mode operation was selected for all subsequent experiments.

To achieve the desired size and location of the ultrasound beam, we simulated various PZT and well dimensions. We also conducted FEM simulations for conventional 6-well, 24-well, and 96-well plates (Fig. S2, Methods). We examine two different parameters: the maximum intensity variation within the organoid space to evaluate uniformity and the ratio of the 90% intensity volume within the organoid space to assess focus location. The FEM simulation results of the former parameter were 89%, 75%, and 53% for 6-well, 24-well, and 96-well plates, respectively. The FEM simulation results of the latter parameter were 23%, 100%, and 94% for the 6-well, 24-well, and 96-well plates, respectively. Therefore, in this work, we used a 24-well plate for all experiments. The resultant beam profile of the 24-well platform operating in the radial mode had a lateral FWHM of 4.9 mm and an axial FWHM of 1 mm. The maximum intensity variation within the organoid space was 72%, and the ratio of the 90% intensity volume within the organoid space was 65%, which was consistent with our FEM simulation results (Fig. 1G, H).

We conducted our experiments in a conventional incubator, which was maintained at a high humidity (~70%) and warm temperature (~37°C). Thus, robust encapsulation of the stimulation platform with a hydrophobic, elastic, and acoustically transparent material was critical for stable, long-term stimulation. After packaging our PUT on the PCB, we dip-coated the entire device in polydimethylsiloxane (PDMS) and measured the electrical impedance throughout multiple experimental cycles in the incubator (Fig. S3, Methods). We confirmed that our device maintained robust operation after nine 6-hour experimental cycles in the incubator. The measured beam profile of six PUTs demonstrated that there was less than 15% variability in the output acoustic intensity (Fig. S4, Methods). This level of consistency was sufficient for successful ultrasound stimulation as demonstrated by our *in vitro* results.

Ultrasound stimulation robustly activates neurons in the organoids.

To investigate whether midbrain organoids were stimulated by ultrasound, we evaluated the gene expression levels and protein levels of cFOS and activation of yes-associated protein (YAP). First, we analyzed the change in cFOS, which is an immediate early gene (IEG) widely used as a biomarker for neural activation (*57*). For US1, the relative mRNA expression of *cFOS* was significantly increased on both MD35 and MD55 (Fig. 2A). cFOS expression for US2 also increased significantly on both MD35 and MD55 (Fig. 2B). In addition to qPCR results, the protein level of cFOS was compared across the experimental groups. Representative immunostaining images exhibited higher levels of cFOS for both MD35 and MD55 across all stimulation conditions compared to the control condition (Fig. 2C, D). Quantitatively, cFOS protein level was significantly increased in US1 on both MD35 and MD55 (Fig. 2E), while there was a slight increase in the protein level of cFOS in US2 on both MD35 and MD55 (Fig. 2F). This discrepancy could have occurred due to the fact that the lower intensity of US2 induced a weaker neuronal response in the mBOs, which is consistent with reports on ultrasound brain stimulation (*51*). These cFOS analysis results implied that US1 successfully stimulated the midbrain organoids.

Next, we observed the translocation of YAP by immunostaining. YAP is one of the transcription coregulators in the Hippo signaling pathway and is activated by various triggers such as the cell density and mechanical cues like the stiffness of the extracellular matrix (ECM). When YAP is activated, phosphorylation of YAP is inhibited, and YAP is translocated into the nucleus. As a mechanical stimulus, ultrasound stimulation is known to be a possible trigger of YAP activation (*58, 59*). Therefore, we analyzed the YAP ratio in the nucleus and cytoplasm using immunostaining techniques. For US1, we observed a slight increase in the ratio of nuclear to cytoplasmic YAP on MD35, while the MD55 organoids demonstrated significantly more YAP translocated into the nucleus (Fig. S5A). For US2, there was no significant change on MD35 and a slight increase on MD55 (Fig. S5B). Representative fluorescence images exhibited higher nuclear translocation of YAP for both MD35 and MD55 across all stimulation conditions compared to the control (Fig. S5C, D).

We also investigated the relative gene expression of the connective tissue growth factor (*CTGF*), which is the downstream target gene of the YAP/TAZ signaling pathway. When the activated YAP is translocated into the nucleus, YAP/TAZ combines with transcriptional enhanced associate domain (TEAD) transcription factor and transcribes downstream target genes such as *CTGF*, cysteine-rich angiogenic inducer 61 (*CYR61*), and amphiregulin (*AREG*). The expression of *CTGF* was increased in US1 organoids on MD35 (Fig. S5E). There was no significant change in *CTGF* in the MD55 organoids. For US2, expression of *CTGF* also significantly increased on MD35, with no changes on MD55 (Fig. S5F). These results confirmed that YAP was activated through both the translocation of YAP and the expression of *CTGF*. Collectively, ultrasound stimulation of midbrain organoids using both conditions successfully activated the mBO cells and regulated the Hippo signaling pathway, which affects the proliferation and differentiation of midbrain organoids. However, as expected, US1 produced a more significant neuronal response in the mBOs, which we mainly attribute to the higher acoustic intensity. These results verified that ultrasound is capable of neural activation in mBOs across several PRFs and acoustic intensities, which was in line with the current reports on ultrasound neuromodulation. Based on these results, we proceeded to investigate the functional responses of mBOs to ultrasound stimulation.

Ultrasound stimulation promotes the induction of dopaminergic progenitor cells.

To determine the functional effects of mBO neuromodulation, we investigated the impact of ultrasound stimulation on critical cellular processes such as differentiation and maturation. Ultrasound was delivered from MD1, with the mBOs already guided into the midbrain lineage (Fig. S6). Since mBOs primarily consist of dopaminergic cell lines, we first investigated the influence of ultrasound stimulation on dopaminergic progenitor cells. By immunostaining the dopaminergic progenitor marker, Forkhead box protein A2 (FOXA2), we verified that FOXA2 levels were significantly increased in organoids stimulated with US1 parameters on MD35 and MD55 (Fig. 3A). For US2, there was a slight increase on both MD35 and MD55 (Fig. 3B). Representative immunostaining images demonstrated higher levels of FOXA2 in both the MD35 and MD55 groups across all conditions compared to the control (Fig. 3C, D). Additional qPCR results demonstrated the relative gene expression level of the LIM homeobox transcription factor 1 alpha (*LMX1A*), which was increased in organoids stimulated with US1 parameters on MD35 and MD55 (Fig. 3E). For US2, there was no change in *LMX1A* levels on MD35, while on MD55, the *LMX1A* level was significantly increased compared to the control (Fig. 3F). These findings suggest that successful ultrasound stimulation causes an increase in the population of dopaminergic progenitor cells, with US1 producing a more significant response. Meanwhile, US2 caused a relatively weaker and delayed increase in dopaminergic progenitor cells, which indicates that temporal modulation of the organoid differentiation stage is parameter dependent. Furthermore, these results were consistent with the cFOS and YAP activation data, which demonstrated that US1 induced a more significant response in the mBOs.

Since ultrasound induced an increase in the population of dopaminergic progenitor cells, we next examined the dopaminergic function of the stimulated mBOs. We analyzed tyrosine hydroxylase (TH), a biomarker for dopaminergic cells, using both protein and gene analysis. First, we evaluated the relative mRNA expression of *TH*. For both US1 and US2, we did not observe any significant changes in *TH* expression levels on MD35 (Fig. 4A). However, a significant decrease in *TH* gene expression was observed for both stimulation conditions on MD55 (Fig. 4B). For the TH protein expression levels, we immunostained for TH (Fig. 4C, D). There were no significant differences between the control and all stimulation conditions on MD35 and MD55 (Fig. 4E, F).

We also assessed the differentiation of the mBO cells into neurons by evaluating the expression levels of both the microtubule-associated protein 2 (*MAP2*) gene and MAP2, a protein marker for neurons. There was no significant difference in both the mRNA expression level of *MAP2* and the protein expression level of MAP2 for both conditions on MD35 and MD55, except for a significant increase in the mRNA *MAP2* expression for US1 on MD55 (Fig. S7A-F). These findings suggested that the ultrasound-induced increase in dopaminergic progenitor cell population slightly inhibited differentiation into dopaminergic cells. This effect was to be expected considering that the overall size of the stimulated mBOs did not increase compared to the control (Fig. S8A, B).

In addition to TH, we quantified the amount of dopamine secretion as a direct barometer of dopaminergic function using an enzyme-linked immunosorbent assay (ELISA). Dopamine levels were slightly decreased on MD35 for both stimulation conditions, while on MD55, dopamine levels were slightly decreased for US1 and significantly decreased for US2 (Fig. S9). These results were consistent with our TH expression data and verified that ultrasound stimulation delivered under these conditions induced population growth into progenitor cells with subtle inhibitory effects on dopaminergic differentiation and function. This effect is a promising approach for noninvasive temporal modulation of early-stage differentiation in organoids.

Ultrasound stimulation modulates transcriptomic signatures.

To confirm the efficient differentiation of hPSCs into mBOs, we conducted transcriptomic comparison between undifferentiated hPSCs and day 35 mBOs. Bulk RNA sequencing data revealed a clear separation between the two groups, with robust induction of neurodevelopmental and region-specific transcriptional programs in mBOs (Fig. S10A). Gene ontology (GO) biological process enrichment analysis of differentially expressed genes (DEGs) exhibited significant enrichment in pathways associated with nervous system development, neuron differentiation, regulation of dopamine secretion, and dopamine metabolic process in the mBO groups (control, US1, US2) (Fig. S10B). KEGG pathway analysis further confirmed the upregulation of dopaminergic synapse, morphine addiction, and oxytocin signaling pathway in mBOs, which are critical for the midbrain (Fig. S10C). In contrast, the hPSCs group exhibited high expression of pluripotency and proliferation-associated genes such as MYC and CDC20, and demonstrated enrichment for cell cycle regulation, DNA replication, and stem cell maintenance pathways. These findings validate the successful and developmentally appropriate differentiation of hPSCs into midbrain lineage by day 35. Importantly, the presence of ultrasound stimulation (US1 or US2) did not disrupt this trajectory, indicating that ultrasound does not compromise differentiation fidelity or lineage identity.

To further investigate the transcriptomic impact of ultrasound stimulation on mBOs, bulk RNA sequencing was performed on organoids subjected to two distinct ultrasound conditions (US1 and US2) and compared to non-stimulated controls (control) at MD35, a timepoint corresponding to early-stage lineage modulation. Principal component analysis (PCA) was conducted to assess the global transcriptomic variance across groups (Fig. 5A). The 3D PCA plot revealed clear separation among the control, US1, and US2 samples along the first three principal

294 components (PC1: 28%, PC2: 26%, PC3: 22%). Each group formed a distinct cluster, which
295 indicated that ultrasound stimulation induced condition-specific transcriptomic profiles. Notably,
296 the separation between US1 and US2 suggested that acoustic intensity and pulse repetition
297 frequency differentially modulated gene expression programs in mBO. Venn diagram analysis
298 revealed that 16 genes were commonly upregulated, and 22 genes were commonly downregulated
299 between US1 and US2. However, each condition also exhibited distinct gene sets, indicating
300 condition-specific transcriptomic responses to ultrasound stimulation (Fig. 5B).
301 Gene ontology (GO) enrichment analysis of differentially expressed genes (DEGs)
302 revealed that US1 induced upregulation of biological processes related to intermediate filament
303 organization, cell–cell signaling, cell adhesion, and epithelial cell differentiation, indicating
304 enhanced structural and developmental maturation (Fig. 5C). In contrast, US2 was associated with
305 enrichment in stress-related and compensatory pathways, including protein refolding, response to
306 immobilization stress, and heat response, suggesting the induction of a stress-adaptive
307 transcriptional program. Gene set enrichment analysis (GSEA) further corroborated these
308 findings. US1 demonstrated significant enrichment of the WNT/β-catenin and mTORC1 signaling
309 pathways compared to the control group, both of which are closely linked to neural development
310 and growth (Fig. 5D). Conversely, US2 demonstrated enrichment in gene sets related to the
311 inflammatory response and unfolded protein response, consistent with cellular stress responses
312 elicited by low-intensity stimulation (Fig. 5E). Despite these condition-specific differences, both
313 ultrasound-treated groups exhibited upregulation of gene sets associated with brain development,
314 accompanied by a consistent downregulation of genes involved in proliferation and cellular
315 damage (Fig. 5F-H). Modular network analysis using MCODE identified a core functional cluster
316 enriched for AP-1 transcription factors, notably cFOS and JUNB, in both conditions, together
317 with co-regulators such as SP1 and EGR1. These results highlight the potential of cFOS-centric
318 regulatory circuits as major drivers of gene expression changes induced by ultrasound stimulation
319 in early organoid differentiation (Fig. 5I, J). Collectively, these results suggested that ultrasound
320 stimulation elicited intensity- and PRF-dependent transcriptional responses in mBOs, likely
321 mediated through the FOS/JUN signaling axis. While US1 promoted gene expression patterns
322 associated with structural maturation and cell adhesion, US2 triggered a stress-tolerant
323 transcriptional state. These findings supported the utility of ultrasound as a tunable biophysical
324 modality for the temporal regulation of organoid differentiation and function.
325
326 **Ultrasound stimulation enhances the synaptic density of dopaminergic neurons in**
327 **organoids.**
328 In order to comprehensively evaluate the effects of ultrasound stimulation on mBOs, we
329 next investigated synaptic density as a marker of cellular maturation. We immunostained for
330 synaptophysin and postsynaptic density protein 95 (PSD95), which are the presynaptic and
331 postsynaptic markers, respectively (Fig. 6A, B). In the case of synaptophysin, there were no
332 significant changes between the control condition and both stimulation conditions for MD35 (Fig.
333 6C, D). On MD55, there was a slight increase in the synaptophysin expression level for both
334 stimulation conditions. On the other hand, there was a slight increase in PSD95 levels on MD35
335 using US1, and a significant increase in PSD95 levels on MD35 using US2 (Fig. 6E, F). On
336 MD55, both conditions produced significantly increased levels of PSD95 in the mBOs. These
337 results demonstrated enhanced organoid maturity due to ultrasound stimulation, with both
338 stimulation conditions generating increased synaptic activity.
339
340 **Ultrasound stimulation reduces cellular damage markers in organoids.**
341 Our stimulation conditions were determined based on established safety guidelines for
342 ultrasound neuromodulation (*60, 61*). Our I_{SPPA}, spatial-peak temporal average intensity (I_{SPTA}),
343 mechanical index (MI), and thermal dose were 500 mW/cm^2, 250 mW/cm^2, 0.306, and 0.00078

344 cumulative equivalent minutes (CEM), respectively, which were sufficiently below the FDA and
345 ITRUSST limits (*60, 61*). The thermal dose was calculated using the measured temperature
346 profile (Fig. S11). To experimentally verify the safety of ultrasound stimulation on mBOs, we
347 conducted quantitative analyses of direct and indirect damage markers. First, we measured the
348 diameter of the mBOs on MD2, MD40, and MD55 to examine the effects of ultrasound
349 stimulation on the overall growth. There was no significant change in diameter between the
350 control and stimulated organoids across all measurements, which confirmed that ultrasound
351 stimulation did not inhibit the overall growth of mBOs (Fig. S8A, B).
352 Next, we examined the protein level of apoptotic and DNA damage markers, cleaved
353 caspase 3 (cC3), p53, and phosphorylated H2A.X (Fig. 7A-D). For cC3, there was a slight
354 decrease in protein levels on MD35, and a significant decrease on MD55 for both US1 and US2
355 (Fig. 7E, F). For p53, there was a slight decrease in protein levels on MD35 for both conditions,
356 while on MD55, only US1 induced a significant decrease in protein levels (Fig. 7G, H). For
357 phosphorylated H2A.X, there was a slight decrease in protein levels for both conditions on both
358 MD35 and MD55 (Fig. 7I, J). These results demonstrated that ultrasound stimulation promoted
359 recovery and neuroprotective effects for both conditions.
360 Last, we quantitatively assessed the differentiation of mBO cells into astrocytes by
361 evaluating the expression levels of the S100 calcium-binding protein B (*S100β*) gene and glial
362 fibrillary acidic protein (GFAP). There was no significant difference in both the mRNA
363 expression level of *S100β* and protein expression level of GFAP for both conditions on MD35 and
364 MD55, except for a significant increase in the *S100β* gene expression for US1 on MD35 (Fig.
365 S12A-F).
366

367 **Discussion**

368 Organoids have become critical biological models that recapitulate the complexity of
369 organs and organ systems. Precisely guiding the differentiation timing of organoids is crucial, and
370 progenitor cells, which are precursors to fully differentiated cells, are critical for therapeutic
371 applications such as tissue grafting and cell transplantation. In this work, we developed a robust
372 multi-well ultrasound stimulation platform for temporal modulation of midbrain organoid (mBO)
373 differentiation. Using two key parameters and comprehensive biomarker analysis, we
374 demonstrated ultrasound-mediated modulation of the dopaminergic progenitor cell population in
375 mBOs. In addition, we verified the importance of PRF and acoustic intensity for stimulation
376 effectiveness and confirmed that ultrasound generally confers a positive effect on mBO growth
377 and maturation.

378 Using our modular stimulation platform, we first investigated the neuronal response of
379 mBOs to ultrasound stimulation by analyzing cFOS and YAP. As expected, both conditions
380 (US1: 500 mW/cm², 3 kHz and US2: 50 mW/cm², 30 Hz) activated the cFOS and YAP
381 mechanisms, which is consistent with previously reported studies. Next, we analyzed the
382 dopaminergic progenitor markers FOXA2 and *LMX1A* to determine the effects of ultrasound on
383 the progenitor population. We verified that US1 was particularly effective in increasing the
384 dopaminergic progenitor population in the mBOs. Interestingly, TH expression and dopamine
385 secretion were reduced at later stages (MD55), suggesting a differentiation delay, thus
386 maintaining progenitor-like states temporarily.

387 Last, we conducted safety assessments using cC3, p53, and phosphorylated H2A.X
388 markers, which are related to apoptosis and DNA damage. Both ultrasound stimulation conditions
389 significantly reduced the expression of all damage markers in the mBOs. Our bulk RNA
390 sequencing results confirmed that the differentiation and maturation of mBOs were largely driven
391 by biochemical cues, with major transcriptomic processes following normal mBO development.
392 The presence of ultrasound stimulation conferred finer control over specific processes related to

cellular mechanics, which was different for US1 and US2. However, we acknowledge that the number of differentially expressed genes (DEGs) was moderate, and the functional interpretation (maturation vs. stress-adaptive pathways) should be viewed as indicative trends that require further validation. Crucially, ultrasound stimulation did not negatively affect mBO growth and indicated that ultrasound stimulation temporally modulated the progenitor differentiation stage via a mechanosensitive pathway.

Regarding the increase in the population of dopaminergic progenitor cells and the expression of genes related to brain development in the stimulated group, the activation of YAP is a possible mediator contributing to these changes (*62-64*). The activation of the JUNB-centered regulatory module, as revealed by network analysis, implicates the involvement of the Hippo and possibly Rho signaling pathways. Given the increased nuclear YAP localization and expression of its downstream target CTGF, our findings align with previous reports linking mechanotransduction to neural progenitor regulation. Although further experiments, such as YAP inhibition or pathway-specific perturbations, are required to establish causality, these observations suggest that ultrasound modulates progenitor cell fate via convergence of FOS/JUN, YAP, and cytoskeletal signaling axes.

Nevertheless, our work suggests that ultrasound safely activates neuronal, astrocytic, and differentiation pathways simultaneously without significantly affecting the overall growth, maturation, and function of other cell types within the mBOs. In particular, we demonstrate temporal modulation of progenitor cell differentiation, which is critical for tissue grafting and transplantation. For successful tissue grafting procedures, 2D and 3D stem or progenitor cell culture systems of a specific organ lineage, including 3D progenitor organoids, have been extensively developed and employed in clinical settings (*12, 13, 65-67*). Such a source of complex differentiated and undifferentiated cells has been traditionally produced using biochemical methods in a free-floating medium. This study presents a potential complementary approach that incorporates ultrasound stimulation to mechanically promote progenitor cell differentiation in an early-stage mBO model.

In addition, we demonstrate the dependence of ultrasound parameters for successful temporal modulation of mBOs, indicating that ultrasound parameter optimization is crucial for developing a therapeutic protocol and that ultrasound induces precise activation of specific pathways. We acknowledge that this research is the beginning of much more work that needs to be conducted to fully understand the effects of ultrasound stimulation on specific cell types during early developmental stages. While this work employs a limited parameter space with only two conditions, our PRFs of 3 kHz and 30 Hz correspond to previous reports of high stimulation success rates and physiologically-relevant gamma frequency bands, respectively (*54, 56, 68*). Our acoustic intensities of 500 mW/cm^2 and 50 mW/cm^2 are an order of magnitude apart and have been implicated in various ultrasound-induced neurological responses both *in vitro* and *in vivo* *(51, 53)*. Another limitation of the current study is the lack of investigation into the reversibility or epigenetic nature of the ultrasound-induced effects in the mBOs. However, based on the reported characteristics of LIFU in the literature, we suggest that our stimulation effects are not permanent (*32, 69*). Further work is necessary to determine the duration of sustained ultrasound-induced effects post-stimulation and whether epigenetic modifications are involved. Nonetheless, our results present a compelling case for using ultrasound stimulation for temporal modulation of differentiation timing in organoids. Future works could build on this study and translate these results to tissue grafting and cell transplantation applications.

Materials and Methods

Experimental design.

This study aimed to investigate the impact of low-intensity focused ultrasound (LIFU) stimulation on midbrain organoid differentiation and maturation. We hypothesized that LIFU stimulation could modulate the timing of cell-type specific differentiation without inducing cellular damage. A modular ultrasound stimulation platform was designed for multi-well compatibility and delivered two stimulation conditions—US1 (500 mW/cm^2, 3 kHz PRF) and US2 (50 mW/cm^2, 30 Hz PRF)—from maturation day 1 (MD1) to MD55. Post-stimulation, organoids were analyzed using immunostaining, qPCR, ELISA, and bulk RNA sequencing to assess neural activation, dopaminergic progenitor cell differentiation, dopaminergic function, synaptic density, and cellular damage markers.

Cell culture and generation of midbrain organoids.

Human embryonic stem cells (hESCs) from the H9 cell line (WiCell Research Institute, Madison, WI, USA) were cultured in mTeSR-1 medium (STEMCELL Technologies) on Matrigel-coated dishes (Corning). The culture medium was refreshed daily, and cells were passaged using ReLeSR (STEMCELL Technologies) according to the manufacturer's instructions. hESC experiments were approved by the Korean MoHW Bioethics Committee (IRB No. P01–201409-ES-01) and followed all applicable ethical guidelines.

Midbrain organoids were generated as previously described [PMID: 36121202], with slight modifications. hESCs were dissociated into single cells using Accutase and seeded at a density of 8×10^3 cells per well in ultra-low attachment 96-well plates to initiate self-organization into embryoid bodies. Upon formation of embryoid bodies, the culture medium was changed to N2 medium composed of a 1:1 mixture of DMEM/F12 and Neurobasal medium supplemented with 1× N2 supplement (Gibco), 1× β-mercaptoethanol, 1% non-essential amino acids (NEAA), 1% penicillin-streptomycin (Pen/Strep), and 1% GlutaMAX. This medium was further supplemented with 10 nM SB431542, 150 ng/ml Noggin, 1.5 μM CHIR99021, and 400 ng/ml sonic hedgehog (SHH), and replaced on days 2, 4, and 6.

On day 8, the medium was changed to N2 medium containing 100 ng/ml fibroblast growth factor 8 (FGF8). On day 11, the culture medium was switched to B27 medium consisting of Neurobasal medium supplemented with 1× B27 supplement without vitamin A (Gibco), 1× β-mercaptoethanol, 1% NEAA, 1% Pen/Strep, and 1% GlutaMAX, further enriched with 100 ng/ml FGF8b, 20 ng/ml brain-derived neurotrophic factor (BDNF), and 200 μM ascorbic acid. From day 14 onward, the organoids were maintained in maturation medium composed of B27 medium supplemented with 20 ng/ml BDNF, 10 ng/ml glial cell-derived neurotrophic factor (GDNF), 200 μM ascorbic acid, 500 μM cyclic AMP (cAMP), and 1 μM DAPT, with fresh factors replenished regularly.

Ultrasound stimulation platform.

The modular PCB was designed (Autodesk Fusion 360, Autodesk, Inc., USA) and fabricated (R&D Tech Co., Ltd, Republic of Korea) for a single-element transducer. A circular lead zirconate titanate (PZT) disk (H4P161000, PZT Electronic Ceramic Co., Ltd, China) with a diameter of 16 mm and a thickness of 2 mm was soldered onto the PCB using a low-temperature solder (SMD291AX, Chip Quik Inc., Canada). An SMA connector (132165, Amphenol RF, USA) was also soldered on the PCB for interfacing with the ultrasound driving circuitry. Then, the assembled PCB was dip-coated with PDMS, which was prepared by mixing the base and curing agent at a 10:1 ratio, and the PZT disk was covered with a polymethylpentene film (PMP, TPX® DX845, Goodfellow Cambridge Ltd., England) for increased robustness. The PDMS was cured on a hotplate at 90°C for at least 4 hours. To evaluate the robustness of the modular platform, the electrical impedance was measured (E4990A, Agilent Technologies Inc., USA) before stimulation and after every other stimulation period for a total of 9 full operation cycles. All measurements were conducted after 6 hours of operation in the incubator.

492
493 **FEM simulation of ultrasound beam**
494 We simulated the ultrasound beam profile for platforms with different PZT diameters,
495 culture well size, and vibration modes of PZT using FEM (COMSOL Multiphysics, MA, USA).
496 To minimize the computation time, we simulated in axisymmetric two dimensions (2D). The
497 geometry of each component, such as culture well, and medium, was set to the same actual size
498 and location. We selected PZT disks with diameters closely matching the bottom size of each well
499 plate. The diameters were set to 35 mm, 16 mm, and 8 mm for 6-well, 24-well, and 96-well
500 plates, respectively.
501 We applied Solid Mechanics, Electrostatics, and Pressure Acoustics, Frequency Domain
502 physics modules. Moreover, the Piezoelectric Effect physics derived from Solid Mechanics and
503 Electrostatics, and Acoustic-Structure Boundary derived from Pressure Acoustics, Frequency
504 Domain, and Solid Mechanics were also added. We applied the terminal voltage at the bottom
505 surface of the PZT disk and grounded the top surface of the PZT disk. We solved these systems
506 with a frequency domain study using a frequency of 73 kHz, 160 kHz, and 320 kHz for radial
507 mode operation in 96-well, 24-well, and 6-well systems, respectively, and 1 MHz for thickness
508 mode operation in 24-well systems. We exported the acoustic intensity magnitude profile into
509 CSV format and processed it with MATLAB software. Using MATLAB software, we plotted a
510 simulated beam profile and 90% intensity contours. We also calculated FWHM, the ratio of the
511 90% intensity volume within the organoid space, and maximum intensity variation within the
512 organoid space.
513
514 **Ultrasound beam profile measurement.**
515 We characterized the ultrasound beam profile of the fabricated platform using a
516 hydrophone (NH0500, Precision Acoustics, UK). The XYZ-location of the hydrophone is
517 precisely controlled by a customized motor system (Sciencetown Inc., Republic of Korea) and a
518 custom-made MATLAB program (Mathworks®, USA) (*41, 56*). The transducer platform was
519 attached beneath the culture well with ultrasound transmission gel. Approximately 500 μL of
520 soybean oil was filled in the culture well, and the hydrophone measured the ultrasound beam
521 profile in the oil by sweeping a cubic volume of 8 mm × 8 mm × 2 mm. The measured voltage
522 signal was amplified and DC-coupled (Precision Acoustics, UK), and the modified signal was
523 acquired with a digital oscilloscope (DSOX2022A, Agilent Technologies, USA). The obtained
524 voltage values were converted to I_{sppa} values by using the following formula.
525 $$I_{SPPA} = {p_{rms}}^2/\rho c,$$
526 where p_{rms} is the root-mean-square pressure, ρ is the density of the media, and c is the
527 speed of sound in the media.
528
529 **Ultrasound stimulation equipment and protocol.**
530 We stimulated midbrain organoids under two different ultrasound conditions and a control
531 condition. The fabricated ultrasound stimulation platform was operated using a function generator
532 (33220A, Agilent Technologies, USA). For both stimulation conditions, the center frequency was
533 fixed at 160 kHz, which corresponds to the radial resonance frequency of the PZT used in this
534 experiment. The ultrasound stimulation was conducted from MD1 to MD55. The duration and
535 duty cycle of ultrasound stimulation were fixed at 10 minutes per 2 days and 50%, respectively,
536 for both conditions. In contrast, the acoustic intensity and PRF were varied. For US1, the acoustic
537 intensity of 500 mW/cm^2 as I_{SPPA} was used with a PRF of 3 kHz. For US2, the acoustic intensity
538 of 50 mW/cm^2 as I_{SPPA} was used with a PRF of 30 Hz. No ultrasound stimulation was delivered
539 for the control condition.
540
541 **Thermal characteristics of the stimulation platform.**

To investigate the heat generation due to ultrasound, we examined the temperature change at the bottom of the well plate. We used the same setup as stimulation, the same well plate, and the same amount of media. The well plate with media was put inside the incubator, and the tip of the thermocouple (T9234, Daihan Scientific Co., Korea) was located at the center of the well plate bottom. Before operating PZT, we waited for temperature stabilization until the temperature had not changed for 10 minutes. We operated PZT with ultrasound US1, and the temperature was measured at 1-minute intervals over 20 minutes. MI and CEM are determined by the following formulas:

$$MI = \frac{P}{\sqrt{f_0}},$$

$$CEM = \int_{t=0}^{t=final} R^{43-T}\, dt,$$

where P is the pressure amplitude, f_0 is the operating frequency, t is the time for the temperature change, and T is the temperature. T was set using the measured profile (Fig. S10), and R was set at 0.25 for $T < 43$°C (*60, 61*).

Immunostaining

For MD1 mBOs, organoids were fixed in 4% paraformaldehyde (PFA) at room temperature for 6 hours and subsequently washed with 1× PBS. Fixed organoids were embedded in optimal cutting temperature (OCT) compound (Tissue-Tek®; Sakura Finetek, USA) and cryosectioned into 7 µm-thick slices using a cryostat (CM1520, Leica, Germany). For immunostaining, sections were permeabilized in 0.3% Triton X-100 (Sigma) in 0.025% TBS-T for 1 hour, followed by blocking with 3% bovine serum albumin (BSA) and 0.02% sodium azide in 0.025% TBS-T for 1 hour at room temperature. Sections were incubated overnight at 4 °C with primary antibodies diluted in blocking buffer: anti-SOX2 (Seven Hills Bioreagents, #WRAB1236), anti-tyrosine hydroxylase (TH; Sigma, #T1299), and anti-MAP2 (R&D Systems, #MAB933). After washing with 1× TBS-T, sections were incubated for 1 hour at room temperature in the dark with Alexa Fluor-conjugated secondary antibodies (Alexa Fluor 488 goat anti-mouse IgG and Alexa Fluor 555 donkey anti-rabbit; Life Technologies) along with Hoechst nuclear stain (Thermo Scientific™). Fluorescent images were acquired using a confocal laser scanning microscope (LSM800, Zeiss, Germany).

Excluding MD1 mBOs, organoids were fixed in 4% paraformaldehyde at room temperature for 5 hours and then washed 3 times with phosphate-buffered saline (PBS), each for 30 minutes. Washed organoids were immersed overnight in a 30% sucrose solution for cryoprotection. Then, the organoids were embedded in an optimal cutting temperature (OCT) compound (Tissue-Tek®; Sakura Finetek, USA) to produce the frozen blocks. Frozen organoids were sectioned into 7-µm-thick slices using a cryocut microtome (CM3050s, Leica, Germany), and sections were obtained from three distinct depths. After drying overnight, sliced samples were washed 3 times with PBS, each for 5 minutes, and permeabilized with 0.3% Triton X-100 in Tris-buffered saline containing 0.025% Tween 20 (TBS-T) solution for 50 minutes. The nonspecific binding of antibodies was blocked with a blocking solution, which contained 3% bovine serum albumin (BSA) and 0.02% sodium azide in 0.025% TBS-T solution for 30 minutes. Primary antibodies were diluted with the blocking solution: anti-phospho-Histone H2A.X (Sigma Aldrich, #05-636), anti-MAP2 (R&D Systems, #MAB8304), anti-p53 (Santa Cruze Biotechnology, #sc-126), anti-PSD95 (Invitrogen, #MA1-046), anti-cC3 (Cell Signaling Technology, #9664s), anti-cFOS (Abcam, ab190289), anti-FOXA2 (Seven Hills Bioreagents, #WRAB1200), anti-GFAP (DAKO, #Z0334), anti-synaptophysin (Abcam, #ab32127), anti-TH (Novus Biologicals, #NB300-109), anti-YAP (Cell Signaling Technology, #14074). Samples were incubated overnight with diluted primary antibodies at 4°C.

Next, samples were washed 3 times with PBS, each for 5 minutes, and incubated with secondary antibodies (Cy3 goat anti-Rabbit IgG; Jackson, Alexa Fluor 555 donkey anti-rabbit;

591 Life Technologies, Alexa Fluor 488 goat anti-mouse IgG; Invitrogen, Alexa Fluor 488 goat anti-
592 mouse IgG; Life Technologies) and Hoechst (Thermo Scientific™) for 1 hour at room
593 temperature in the dark. Again, samples were washed 3 times with PBS for 5 minutes each. The
594 slide glass with stained samples was covered with a coverslip after dropping the mounting
595 solution. Stained samples were observed under a confocal microscope (LSM980, Zeiss, Germany
596 / AX, Nikon, Japan) and analyzed with ImageJ software (National Institutes of Health, Bethesda,
597 MD, United States).
598
599 **Real-time PCR**
600 Total RNA was extracted from organoids using the easy-BLUE™ Total RNA Extraction
601 Kit (iNtRON Biotechnology) following washing with 1× PBS. RNA was purified through
602 chloroform and isopropanol precipitation, and the resulting RNA pellet was washed with cold
603 70% ethanol. RNA concentration was determined using a NanoDrop spectrophotometer (Thermo
604 Fisher Scientific). A total of 1200 ng RNA was reverse transcribed into complementary DNA
605 (cDNA) using the SuperScript IV Reverse Transcriptase kit (Thermo Fisher Scientific).
606 Quantitative real-time PCR was performed using Fast SYBR™ Green PCR Master Mix (Applied
607 Biosystems) and gene-specific primers to evaluate marker gene expression levels.
608
609 **Dopamine ELISA**
610 Cultured medium was collected 24 hours after incubation from each well of a 24-well
611 plate, containing a single organoid. Collected medium was analyzed using a dopamine ELISA kit
612 (ENZ-KIT188, Enzo, Switzerland) according to the instructions of the manufacturer. Each sample
613 was added to a plate well, and the same volume of biotin-detection antibody working solution was
614 added. The plate was incubated for 45 minutes at 37°C and washed. After washing, horseradish
615 peroxidase (HRP)-streptavidin working solution was added into each well and incubated for 30
616 minutes at 37°C. The plate was washed again, and tetramethylbenzidine (TMB) substrate was
617 added. The plate was then incubated in the dark for 15 minutes at 37°C. After incubation, a stop
618 solution was added immediately. The optical density absorbance at 450 nm was measured by a
619 microplate reader (#EPOCH-SN, Agilent, CA, United States). Dopamine concentration of
620 samples was calculated with a standard curve using GraphPad Prism software 6.0 (GraphPad
621 Software, Inc., CA, United States).
622
623 **Bulk RNA sequencing**
624 To comprehensively assess gene expression profiles in midbrain organoids, bulk RNA
625 sequencing was performed by Macrogen (Seoul, Korea). Samples were collected from four
626 experimental groups, including PSC, mBO-control, US1, and US2 at day 35 of differentiation
627 (MD35). RNA libraries were prepared using the TruSeq Stranded mRNA LT Sample Prep Kit
628 (Illumina, San Diego, CA, USA), and sequencing was conducted on an Illumina platform. Raw
629 sequencing reads were subjected to quality trimming and aligned to the human reference genome
630 (GRCh38) using HISAT2. Transcript assembly was carried out with StringTie, and transcript
631 abundance was quantified in fragments per kilobase of transcript per million mapped reads
632 (FPKM). Expression data were further normalized by $\log_2$ transformation [$\log_2$(FPKM + 1)] prior
633 to downstream analyses. Gene set enrichment analysis (GSEA) was conducted using GSEA
634 Desktop v4.3.3 (Broad Institute) with all type signature gene sets from the Human MSigDB
635 Collections (v2024). Pearson correlation coefficients (r) between samples from each group
636 (control, US1, and US2) were independently calculated using ExDEGA v5.2.1. Differentially
637 expressed genes (DEGs) were filtered based on a fold-change threshold of 2 on PSC-mBO
638 comparison and >1.5 or <0.7 on ultrasound stimulation comparison, and visualized by heatmap
639 generation in MeV 4.9.0. Pathway enrichment analyses were conducted using the DAVID
640 Bioinformatics Resources v6.8 (https://david.ncifcrf.gov) and the Reactome database

(https://reactome.org/), including MCODE. Resulting pathway networks were visualized and further analyzed using Cytoscape software (www.cytoscape.org).

Statistical analysis

Normal distribution of all *in vitro* data sets was confirmed using the Shapiro-Wilk test. For immunohistology data and RT-PCR data, a two-sample two-sided unpaired Student's *t*-test was conducted on normally distributed data. For non-parametric data, the Mann-Whitney U test was used. For ELISA data, a one-sample two-sided Student's *t*-test against a value of 1 was conducted. All data were analyzed using Microsoft Excel (Microsoft Co., WA, USA), OriginPro 2019 (OriginLab Co., MA, USA), and MATLAB R2022b (Mathworks, MA, USA). Unless stated otherwise, all data are presented as mean ± standard deviation (SD), and a p-value of <0.05 was considered significant. Graphical illustrations of biological components in all relevant figures were created with Adobe Illustrator 2023 and BioRender.com.

References

1. M. Hofer, M. P. Lutolf, Engineering organoids. *Nat Rev Mater* **6**, 402-420 (2021).
2. J. C. Park *et al.*, A logical network-based drug-screening platform for Alzheimer's disease representing pathological features of human brain organoids. *Nat Commun* **12**, 280 (2021).
3. M. N. Wilson *et al.*, Multimodal monitoring of human cortical organoids implanted in mice reveal functional connection with visual cortex. *Nat Commun* **13**, 7945 (2022).
4. S. Jeon *et al.*, Recent advances in endocrine organoids for therapeutic application. *Adv Drug Deliv Rev* **199**, 114959 (2023).
5. C. Li *et al.*, Single-cell brain organoid screening identifies developmental defects in autism. *Nature* **621**, 373-380 (2023).
6. Y. Lee, J. S. Kang, O. J. Ham, M. Y. Son, M. O. Lee, Gut metabolite trimethylamine N-oxide induces aging-associated phenotype of midbrain organoids for the induced pluripotent stem cell-based modeling of late-onset disease. *Front Aging Neurosci* **14**, 925227 (2022).
7. J. S. Kang *et al.*, Generation of induced alveolar assembloids with functional alveolar-like macrophages. *Nat Commun* **16**, 3346 (2025).
8. G. Maisumu *et al.*, Brain organoids: building higher-order complexity and neural circuitry models. *Trends Biotechnol*, (2025).
9. G. Rossi, A. Manfrin, M. P. Lutolf, Progress and potential in organoid research. *Nat Rev Genet* **19**, 671-687 (2018).
10. S. Scuderi *et al.*, Specification of human brain regions with orthogonal gradients of WNT and SHH in organoids reveals patterning variations across cell lines. *Cell Stem Cell* **32**, 970-989 e911 (2025).
11. A. Pagliaro *et al.*, Temporal morphogen gradient-driven neural induction shapes single expanded neuroepithelium brain organoids with enhanced cortical identity. *Nat Commun* **14**, 7361 (2023).
12. B. M. Hiller *et al.*, Optimizing maturity and dose of iPSC-derived dopamine progenitor cell therapy for Parkinson's disease. *NPJ Regen Med* **7**, 24 (2022).
13. D. Doi *et al.*, Pre-clinical study of induced pluripotent stem cell-derived dopaminergic progenitor cells for Parkinson's disease. *Nat Commun* **11**, 3369 (2020).
14. D. A. Shear *et al.*, Neural progenitor cell transplants promote long-term functional recovery after traumatic brain injury. *Brain Res* **1026**, 11-22 (2004).
15. M. A. Cadena *et al.*, A 3D Bioprinted Cortical Organoid Platform for Modeling Human Brain Development. *Adv Healthc Mater* **13**, e2401603 (2024).
16. S. A. Yi, Y. Zhang, C. Rathnam, T. Pongkulapa, K. B. Lee, Bioengineering Approaches for the Advanced Organoid Research. *Adv Mater* **33**, e2007949 (2021).

17. S. L. Giandomenico *et al.*, Cerebral organoids at the air-liquid interface generate diverse nerve tracts with functional output. *Nat Neurosci* **22**, 669-679 (2019).
18. X. Qian *et al.*, Generation of human brain region-specific organoids using a miniaturized spinning bioreactor. *Nat Protoc* **13**, 565-580 (2018).
19. V. Velasco, S. A. Shariati, R. Esfandyarpour, Microtechnology-based methods for organoid models. *Microsyst Nanoeng* **6**, 76 (2020).
20. X. Qian *et al.*, Sliced Human Cortical Organoids for Modeling Distinct Cortical Layer Formation. *Cell Stem Cell* **26**, 766-781 e769 (2020).
21. M. O'Hara-Wright, S. Mobini, A. Gonzalez-Cordero, Bioelectric Potential in Next-Generation Organoids: Electrical Stimulation to Enhance 3D Structures of the Central Nervous System. *Front Cell Dev Biol* **10**, 901652 (2022).
22. T. Kwak *et al.*, Guidelines for Manufacturing and Application of Organoids: Brain. *Int J Stem Cells* **17**, 158-181 (2024).
23. C. Wu *et al.*, A Bioactive and Photoresponsive Platform for Wireless Electrical Stimulation to Promote Neurogenesis. *Adv Healthc Mater* **11**, e2201255 (2022).
24. I. C. Lee, Y. C. Lin, H. L. Liu, N. C. Liu, Dual-frequency ultrasound enhances functional neuron differentiation from neural stem cells by modulating Ca(2+) dynamics and the ERK1/2 signaling pathway. *J Cell Physiol* **238**, 137-150 (2023).
25. S. Yoo, D. R. Mittelstein, R. C. Hurt, J. Lacroix, M. G. Shapiro, Focused ultrasound excites cortical neurons via mechanosensitive calcium accumulation and ion channel amplification. *Nat Commun* **13**, 493 (2022).
26. Y. Yang *et al.*, Induction of a torpor-like hypothermic and hypometabolic state in rodents by ultrasound. *Nat Metab* **5**, 789-803 (2023).
27. C. Kong *et al.*, Long-lasting restoration of memory function and hippocampal synaptic plasticity by focused ultrasound in Alzheimer's disease. *Brain Stimul* **16**, 857-866 (2023).
28. Y. Wu *et al.*, Low-intensity pulsed ultrasound regulates proliferation and differentiation of neural stem cells through notch signaling pathway. *Biochem Biophys Res Commun* **526**, 793-798 (2020).
29. M. F. Villamar, A. Santos Portilla, F. Fregni, R. Zafonte, Noninvasive brain stimulation to modulate neuroplasticity in traumatic brain injury. *Neuromodulation* **15**, 326-338 (2012).
30. K. R. Murphy *et al.*, Optimized ultrasound neuromodulation for non-invasive control of behavior and physiology. *Neuron* **112**, 3252-3266 e3255 (2024).
31. L. Liang *et al.*, Piezotronic effect determined neuron-like differentiation of adult stem cells driven by ultrasound. *Nano Energy* **90**, (2021).
32. D. P. Darrow, P. O'Brien, T. J. Richner, T. I. Netoff, E. S. Ebbini, Reversible neuroinhibition by focused ultrasound is mediated by a thermal mechanism. *Brain Stimul* **12**, 1439-1447 (2019).
33. A. Bargero *et al.*, Ultrasound-Responsive Polymeric Piezoelectric Nanoparticles for Remote Activation and Neuronal Differentiation of Human Neural Stem Cells. *Small Sci* **5**, 2400354 (2025).
34. T. Riis, D. Feldman, B. Mickey, J. Kubanek, Controlled noninvasive modulation of deep brain regions in humans. *Communications Engineering* **3**, (2024).
35. S. Kim, N. Kwon, M. M. Hossain, J. Bendig, E. E. Konofagou, Displacement and functional ultrasound (fUS) imaging of displacement-guided focused ultrasound (FUS) neuromodulation in mice. *Neuroimage* **298**, 120768 (2024).
36. S. S. Yoo *et al.*, Focused ultrasound modulates region-specific brain activity. *Neuroimage* **56**, 1267-1275 (2011).
37. Y. Jo *et al.*, General-Purpose Ultrasound Neuromodulation System for Chronic, Closed-Loop Preclinical Studies in Freely Behaving Rodents. *Advanced Science* **9**, (2022).

38. T. Di Ianni *et al.*, High-throughput ultrasound neuromodulation in awake and freely behaving rats. *Brain Stimul* **16**, 1743-1752 (2023).
39. J. Zhu *et al.*, The mechanosensitive ion channel Piezo1 contributes to ultrasound neuromodulation. *Proc Natl Acad Sci U S A* **120**, e2300291120 (2023).
40. H. Kim *et al.*, Miniature ultrasound ring array transducers for transcranial ultrasound neuromodulation of freely-moving small animals. *Brain Stimulation* **12**, 251-255 (2019).
41. S. Kim *et al.*, Miniaturized MR-compatible ultrasound system for real-time monitoring of acoustic effects in mice using high-resolution MRI. *NeuroImage* **276**, (2023).
42. G. Kook *et al.*, Multifocal skull-compensated transcranial focused ultrasound system for neuromodulation applications based on acoustic holography. *Microsystems & Nanoengineering* **9**, (2023).
43. S. Kim *et al.*, Transcranial focused ultrasound stimulation with high spatial resolution. *Brain Stimulation* **14**, 290-300 (2021).
44. Y. Tufail *et al.*, Transcranial pulsed ultrasound stimulates intact brain circuits. *Neuron* **66**, 681-694 (2010).
45. Y. Tufail, A. Yoshihiro, S. Pati, M. M. Li, W. J. Tyler, Ultrasonic neuromodulation by brain stimulation with transcranial ultrasound. *Nat Protoc* **6**, 1453-1470 (2011).
46. K. Lee *et al.*, Ultrasonocoverslip: In-vitro platform for high-throughput assay of cell type-specific neuromodulation with ultra-low-intensity ultrasound stimulation. *Brain Stimul* **16**, 1533-1548 (2023).
47. X. H. Li *et al.*, Low-intensity ultrasound ameliorates brain organoid integration and rescues microcephaly deficits. *Brain* **147**, 3817-3833 (2024).
48. J. Kubanek *et al.*, Stem cell-derived brain organoids for controlled studies of transcranial neuromodulation. *Heliyon* **9**, e18482 (2023).
49. B. R. Kop *et al.*, Auditory confounds can drive online effects of transcranial ultrasonic stimulation in humans. *Elife* **12**, (2024).
50. A. K. Zadeh *et al.*, The effect of transcranial ultrasound pulse repetition frequency on sustained inhibition in the human primary motor cortex: A double-blind, sham-controlled study. *Brain Stimul* **17**, 476-484 (2024).
51. R. L. King, J. R. Brown, W. T. Newsome, K. B. Pauly, Effective parameters for ultrasound-induced in vivo neurostimulation. *Ultrasound Med Biol* **39**, 312-331 (2013).
52. K. Zeng *et al.*, Effects of different sonication parameters of theta burst transcranial ultrasound stimulation on human motor cortex. *Brain Stimul* **17**, 258-268 (2024).
53. H. Kim, A. Chiu, S. D. Lee, K. Fischer, S. S. Yoo, Focused ultrasound-mediated non-invasive brain stimulation: examination of sonication parameters. *Brain Stimul* **7**, 748-756 (2014).
54. K. Yu, X. Niu, E. Krook-Magnuson, B. He, Intrinsic functional neuron-type selectivity of transcranial focused ultrasound neuromodulation. *Nat Commun* **12**, 2519 (2021).
55. T. Nandi, B. R. Kop, K. Butts Pauly, C. J. Stagg, L. Verhagen, The relationship between parameters and effects in transcranial ultrasonic stimulation. *Brain Stimul* **17**, 1216-1228 (2024).
56. Y. Jo *et al.*, Selective manipulation of excitatory and inhibitory neurons in top-down and bottom-up visual pathways using ultrasound stimulation. *Brain Stimul* **18**, 848-862 (2025).
57. M. Dragunow, R. Faull, The Use of C-Fos as a Metabolic Marker in Neuronal Pathway Tracing. *J Neurosci Meth* **29**, 261-265 (1989).
58. A. Elosegui-Artola *et al.*, Force Triggers YAP Nuclear Entry by Regulating Transport across Nuclear Pores. *Cell* **171**, 1397-1410 e1314 (2017).
59. X. M. Xu *et al.*, Low-Intensity Pulsed Ultrasound Treatment Accelerates Angiogenesis by Activating YAP/TAZ in Human Umbilical Vein Endothelial Cells. *Ultrasound Med Biol* **44**, 2655-2661 (2018).

60. J.-F. Aubry *et al.*, ITRUSST consensus on biophysical safety for transcranial ultrasonic stimulation. *arXiv preprint arXiv:2311.05359*, (2023).
61. E. Martin *et al.*, ITRUSST consensus on standardised reporting for transcranial ultrasound stimulation. *Brain Stimul* **17**, 607-615 (2024).
62. D. Guo *et al.*, The Critical Role of YAP/BMP/ID1 Axis on Simulated Microgravity-Induced Neural Tube Defects in Human Brain Organoids. *Adv Sci (Weinh)* **12**, e2410188 (2025).
63. A. Lavado *et al.*, The Hippo Pathway Prevents YAP/TAZ-Driven Hypertranscription and Controls Neural Progenitor Number. *Dev Cell* **47**, 576-591 e578 (2018).
64. A. Jain *et al.*, Morphodynamics of human early brain organoid development. *Nature*, (2025).
65. S. Y. Cao *et al.*, Cerebral organoids transplantation repairs infarcted cortex and restores impaired function after stroke. *NPJ Regen Med* **8**, 27 (2023).
66. K. W. Kelley *et al.*, Host circuit engagement of human cortical organoids transplanted in rodents. *Nat Protoc* **19**, 3542-3567 (2024).
67. O. Revah *et al.*, Maturation and circuit integration of transplanted human cortical organoids. *Nature* **610**, 319-326 (2022).
68. H. J. Kim *et al.*, Long-lasting forms of plasticity through patterned ultrasound-induced brainwave entrainment. *Sci Adv* **10**, (2024).
69. P. Pouget *et al.*, Neuronavigated Repetitive Transcranial Ultrasound Stimulation Induces Long-Lasting and Reversible Effects on Oculomotor Performance in Non-human Primates. *Front Physiol* **11**, 1042 (2020).

Acknowledgments

We would like to acknowledge the facilities and the scientific and technical assistance of the KARA (KAIST Analysis Center for Research Advancement), KAIST Bio Core Center, and Microscopy and Imaging Analysis Core Facility in the BioMedical Research Center (BMRC), KAIST. We also thank S. Bang for his comments on the graphical illustrations.

Funding:
K-Brain Project of the National Research Foundation (NRF) funded by the Korean government (MSIT) RS-2023-00262568 (HJL)
Korea Dementia Research Project through the Korea Dementia Research Center (KDRC), funded by the Ministry of Health & Welfare and Ministry of Science and ICT, Republic of Korea RS-2024-00355871 (HJL)
BK21 FOUR Connected AI Education & Research Program for Industry and Society Innovation, KAIST EE, No. 4120200113769 (HJL)
Korea Research Institute of Bioscience and Biotechnology (KRIBB) Research Initiative Program KGM4722533 (M-OL)

Author contributions:

Conceptualization: JJ, YJ, EJ, HJL
Methodology: JJ, YJ, YL, M-OL, HJL
Investigation: JJ, YJ, YL, EJ
Visualization: JJ, YJ, YL
Resource: JJ, YJ, YL, YJ, WDH, M-OL, HJL
Validation: JJ, YJ, YL
Formal analysis: JJ, YJ, JHS

Supervision: M-OL, HJL
Writing—original draft: JJ, YJ, YL, M-OL, HJL
Writing—review & editing: JJ, YJ, YL, YJ, WDH, JHS, M-OL, HJL

Competing interests: Authors declare that they have no competing interests.

Data and materials availability: All data are available in the main text or the supplementary materials.

Figures and Tables

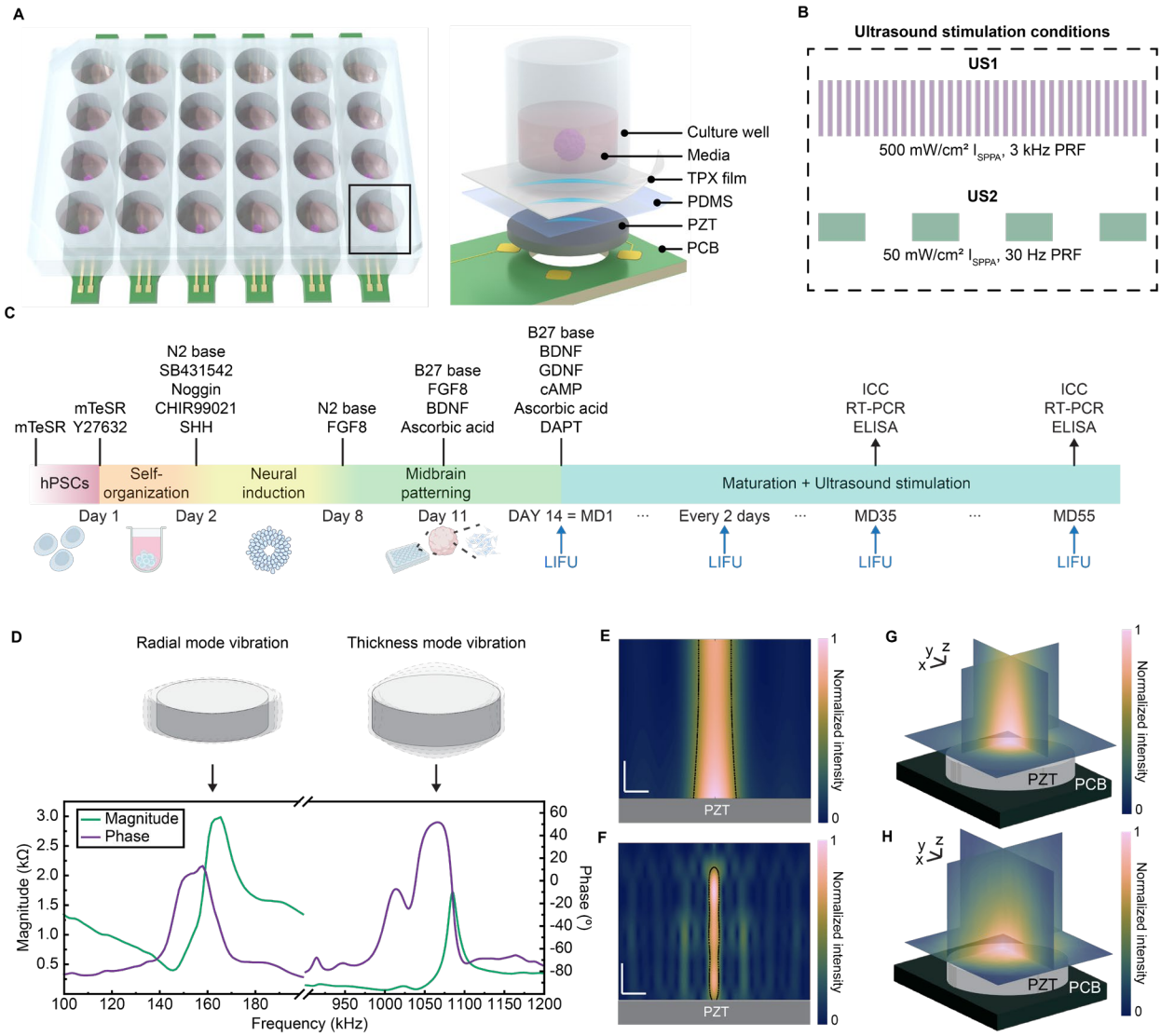

Fig. 1. Ultrasound stimulation of midbrain organoids. (**A**) Schematic illustration of the ultrasound stimulation platform. (**B**) The ultrasound waveform used to stimulate midbrain organoids. (**C**) Timeline for generation of midbrain organoids and ultrasound stimulation**.** (**D**) Impedance of the two different resonance modes. (**E and F**) Simulated beam profile generated by operating PZT discs in two different resonance modes. Scale bar, 0.5 mm (vertical) and 2 mm (horizontal). (**G**) Simulated 3D beam profile produced by operating a PZT disc in the radial

resonance mode. Scale bar, 1 mm (x-axis), 1 mm (y-axis), and 0.1 mm (z-axis). (**H**) Measured 3D beam profile produced by operating a PZT disc in the radial resonance mode. Scale bar, 1 mm (x-axis), 1 mm (y-axis), and 0.1 mm (z-axis).

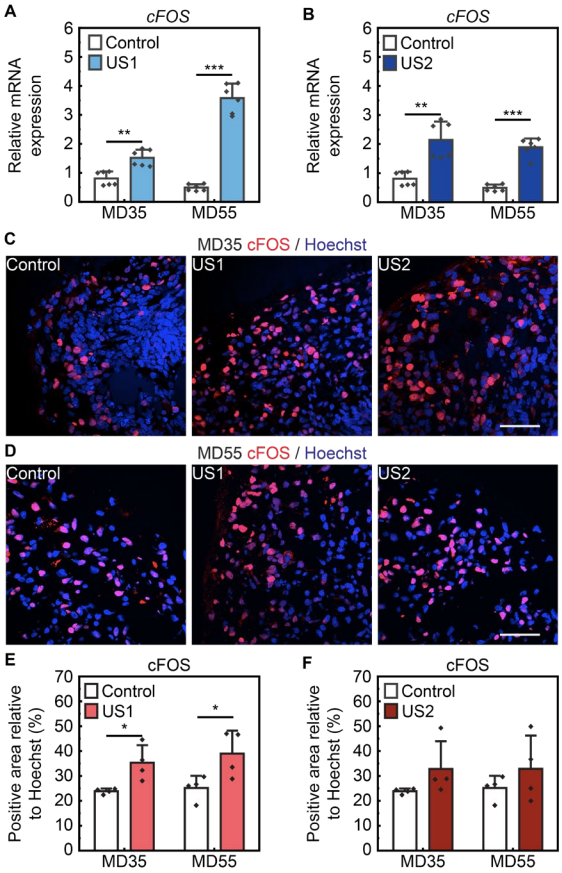

Fig. 2. Activation of neural cells by ultrasound stimulation using two conditions. (**A**) Relative mRNA expression of *cFOS* in the US1 group. MD35, Mann-Whitney U test, U=0, **p<0.01, n=6. MD55, two sample two-sided unpaired Student's t-test, t=-14.70, ***p<0.001, n=6. (**B**) Relative mRNA expression of *cFOS* in the US2 group. MD35, Mann-Whitney U test, U=0, **p<0.01, n=6. MD55, two sample two-sided unpaired Student's t-test, t=-10.50, ***p<0.001, n=6. (**C and D**) Representative immunostaining images of cFOS. Scale bar, 50 µm. (**E**) Relative protein level of cFOS in the US1 group. MD35, two sample two-sided unpaired Student's t-test, t=-3.210, *p<0.05, n=4. MD55, two sample two-sided unpaired Student's t-test, t=-2.654, *p<0.05, n=4. (**F**) Relative protein level of cFOS in the US2 group. MD35, two sample two-sided unpaired Student's t-test, t=–1.598, p=0.207, n=4. MD55, two sample two-sided unpaired Student's t-test, t=-1.090, p=0.340, n=4. Solid bars and error bars indicate mean value and standard deviation, respectively.

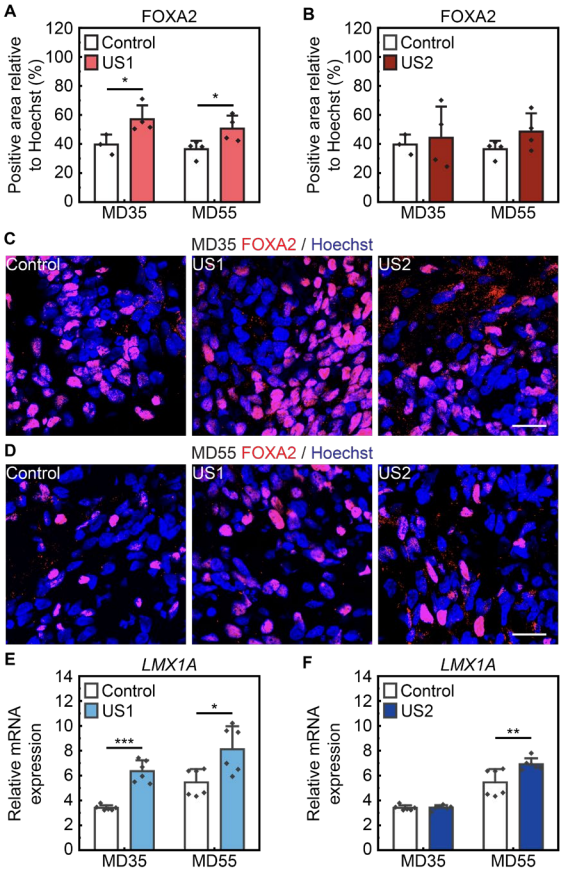

Fig. 3. Controlled differentiation of dopaminergic progenitor cells using ultrasound stimulation. (**A**) Relative protein level of FOXA2 in the US1 group. MD35, two sample two-sided unpaired Student's t-test, t=–2.800, *p<0.05, n=4. MD55, two sample two-sided unpaired Student's t-test, t=–2.674, *p<0.05, n=4. (**B**) Relative protein level of FOXA2 in the US2 group. MD35, two sample two-sided unpaired Student's t-test, t=–0.411, p=0.703, n=4. MD55, two sample two-sided unpaired Student's t-test, t=–1.733, p=0.155, n=4. (**C and D**) Representative immunostaining images of FOXA2. Scale bar, 20 µm. (**E**) Relative mRNA expression of *LMX1a* in the US1 group. MD35, two sample two-sided unpaired Student's t-test, t=–7.979, ***p<0.001, n=6. MD55, Mann-Whitney U test, U=4, *p<0.05, n=6. (**F**) Relative mRNA expression of *LMX1a* in the US2 group. MD35, two sample two-sided unpaired Student's t-test, t=–0.186, p=0.856, n=6. MD55, Mann-Whitney U test, U=1, **p<0.01, n=6.

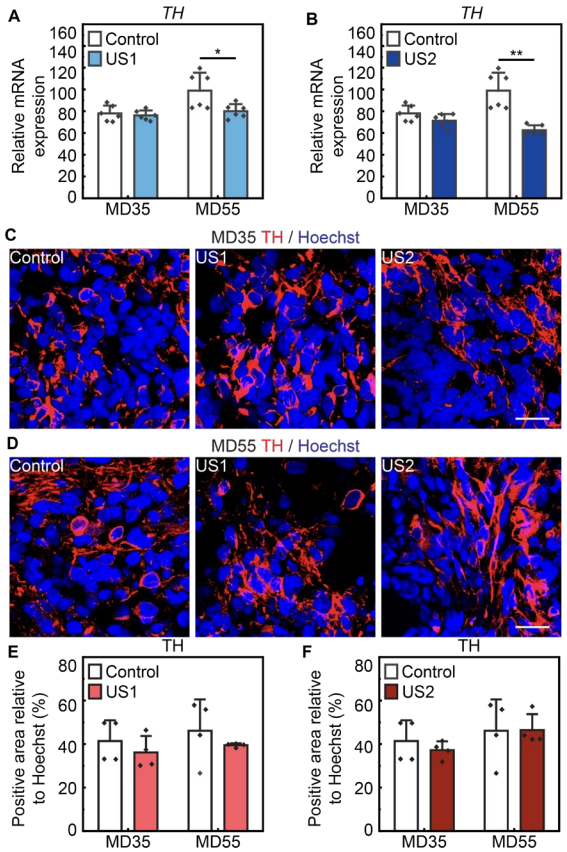

Fig. 4. Controlled differentiation of dopaminergic neurons using ultrasound stimulation. (**A**) Relative mRNA expression of *TH* in the US1 group. MD35, two sample two-sided unpaired Student's *t*-test, t=0.519, p=0.617, n=6 . MD55, two sample two-sided unpaired Student's *t*-test, t=2.586, *p<0.05, n=6. (**B**) Relative mRNA expression of *TH* in the US2 group. MD35, two sample two-sided unpaired Student's *t*-test, t=1.726, p=0.116, n=6 . MD55, two sample two-sided unpaired Student's *t*-test, t=5.184, **p<0.01, n=6. (**C and D**) Representative immunostaining images of TH. Scale bar, 20 µm. (**E**) Relative protein level of TH in the US1 group. MD35, Mann-Whitney U test, U=12, p=0.343, n=4. MD55, two sample two-sided unpaired Student's *t*-test, t=0.925, p=0.423, n=4. (**F**) Relative protein level of TH in the US2 group. MD35, Mann-Whitney U test, U=10, p=0.686, n=4. MD55, Mann-Whitney U test, U=10, p=0.686, n=4.

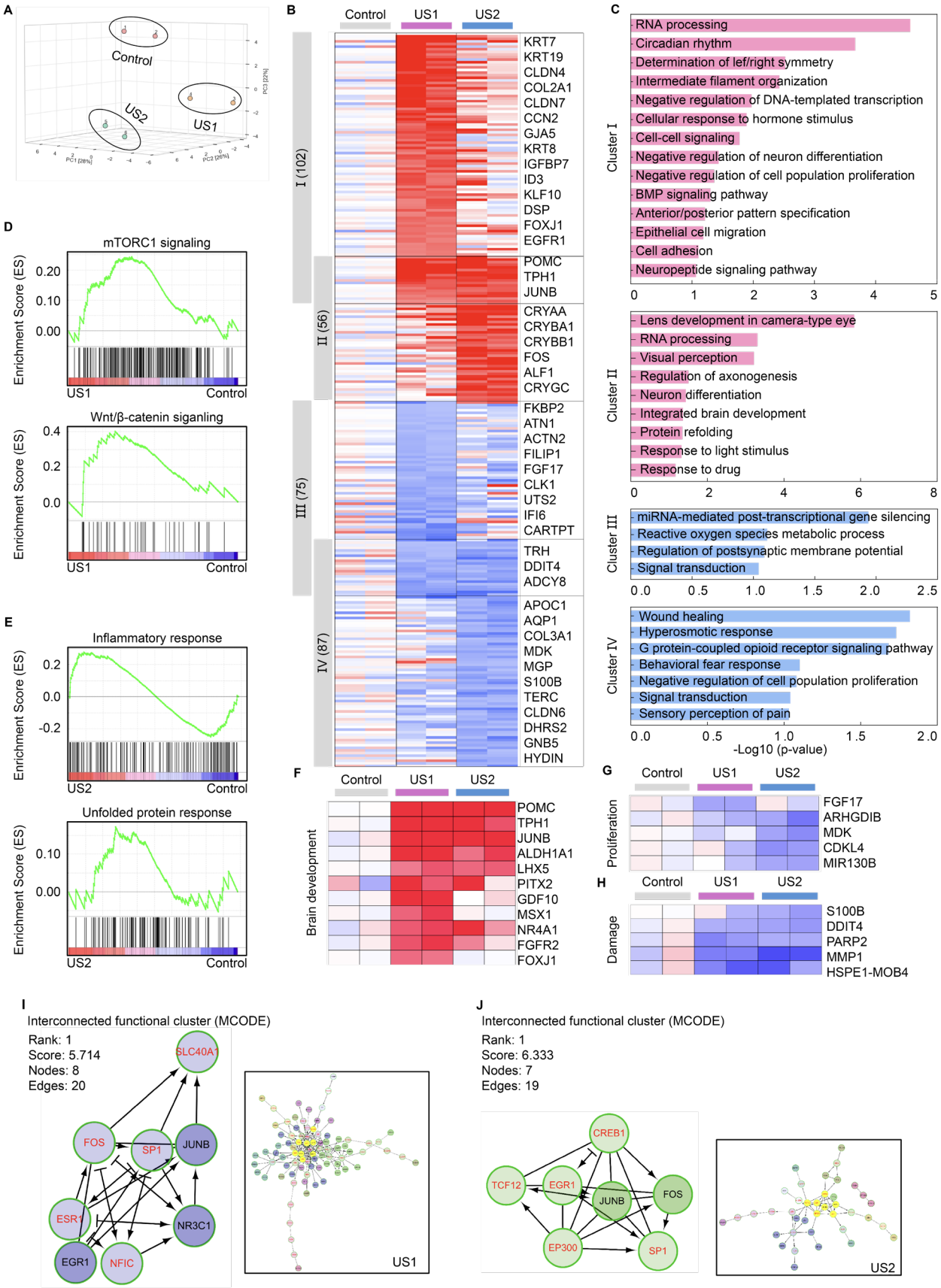

Fig. 5. Total transcriptome analysis. (**A**) 3D PCA plot of three different groups. (**B**) Heatmap plot of DEGs. (**C**) GO analysis results of each cluster. (**D**) Enrichment

plot of the mTORC1 signaling and WNT/β-catenin signaling in US1. (**E**) Enrichment plot of the inflammatory response and unfolded protein response in US2. (**F**), Heatmap of genes related to brain development. (**G**) Heatmap of genes related to the proliferation. (**H**) Heatmap of genes related to the damage. (**I**) MCODE analysis of the US1 group. (**J**) MCODE analysis of the US2 group.

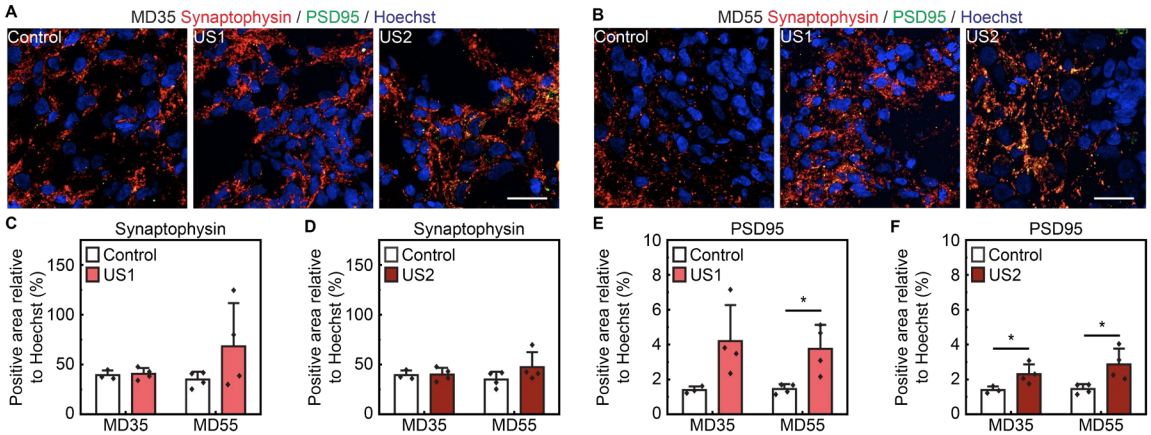

Fig. 6. Controlled synaptic density of midbrain organoids using ultrasound stimulation. (**A and B**) Representative immunostaining images of synaptophysin and PSD95. Scale bar, 50 μm. (**C**) Relative protein level of synaptophysin in the US1 group. MD35, two sample two-sided unpaired Student's *t*-test, t=-0.323, p=0.760, n=4. MD55, two sample two-sided unpaired Student's *t*-test, t=-1.510, p=0.223, n=4. (**D**) Relative protein level of synaptophysin in the US2 group. MD35, two sample two-sided unpaired Student's *t*-test, t=-0.140, p=0.894, n=4. MD55, two sample two-sided unpaired Student's *t*-test, t=-1.467, p=0.208, n=4. (**E**) Relative protein level of PSD95 in the US1 group. MD35, two sample two-sided unpaired Student's *t*-test, t=–2.694, p=0.072, n=4. MD55, two sample two-sided unpaired Student's *t*-test, t = -3.283, *p<0.05, n=4. (**F**) Relative protein level of PSD95 in the US2 group. MD35, two sample two-sided unpaired Student's *t*-test, t=-2.936, *p<0.05, n=4. MD55, two sample two-sided unpaired Student's *t*-test, t = -2.964, *p<0.05, n=4. Solid bars and error bars indicate mean value and standard deviation, respectively.

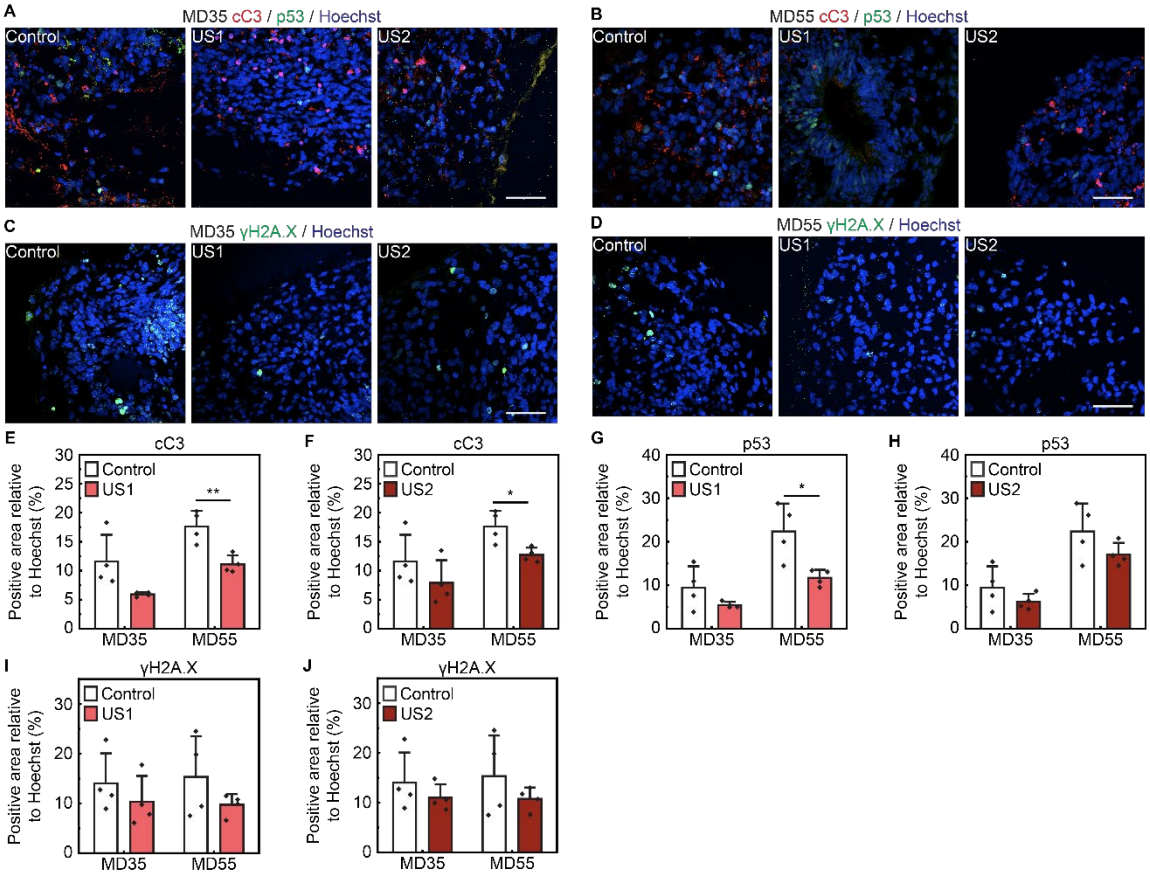

Fig. 7. Safety evaluation of ultrasound stimulation on midbrain organoids. (**A and B**) Representative immunostaining images of cC3 and p53. Scale bar, 50 µm. (**C**) Relative protein level of cC3 in the US1 group. MD35, two sample two-sided unpaired Student's *t*-test, t=2.447, p=0.091, n=4. MD55, two sample two-sided unpaired Student's *t*-test, t=4.179, $^{**}p<0.01$, n=4. (**D**) Relative protein level of cC3 in the US2 group. MD35, two sample two-sided unpaired Student's *t*-test, t=1.214, p=0.272, n=4. MD55, two sample two-sided unpaired Student's *t*-test, t=3.281, $^{*}p<0.05$, n=4. (**E**) Relative protein level of p53 in the US1 group. MD35, two sample two-sided unpaired Student's *t*-test, t=1.604, p=0.204, n=4. MD55, two sample two-sided unpaired Student's *t*-test, t=3.192, $^{*}p<0.05$, n=4 (**F**) Relative protein level of p53 in the US2 group. MD35, two sample two-sided unpaired Student's *t*-test, t=1.238, p=0.287, n=4. MD55, two sample two-sided unpaired Student's *t*-test, t=1.526, p=0.201, n=4. (**G and H**) Representative immunostaining images of phosphorylated H2A.X. Scale bar, 50 µm. (**I**) Relative protein level of phosphorylated H2A.X in the US1 group. MD35, two sample two-sided unpaired Student's *t*-test, t=0.921, p=0.393, n=4. MD55, two sample two-sided unpaired Student's *t*-test, t=1.327, p=0.266, n=4. (**J**) Relative protein level of phosphorylated H2A.X in the US2 group. MD35, two sample two-sided unpaired Student's *t*-test, t=0.914, p=0.411, n=4. MD55, two sample two-sided unpaired Student's *t*-test, t=1.078, p=0.350, n=4.

Supplementary Materials

Figs. S1 to S12 (separate file)
Data S1 and S2 (separate files)

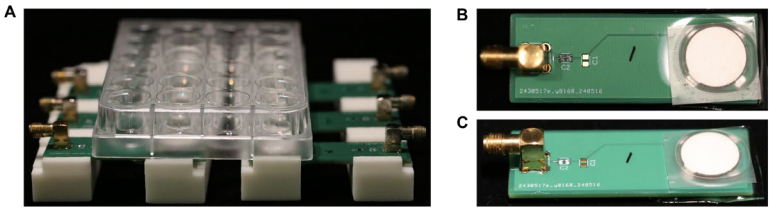

Fig. S1. Photos of ultrasound transducer platforms. (**A**) Integration of 24-well plates and six ultrasound transducer platforms placed inside the incubator. (**B**) Top view of a single ultrasound transducer platform. (**C**) Front view of the ultrasound transducer platform.

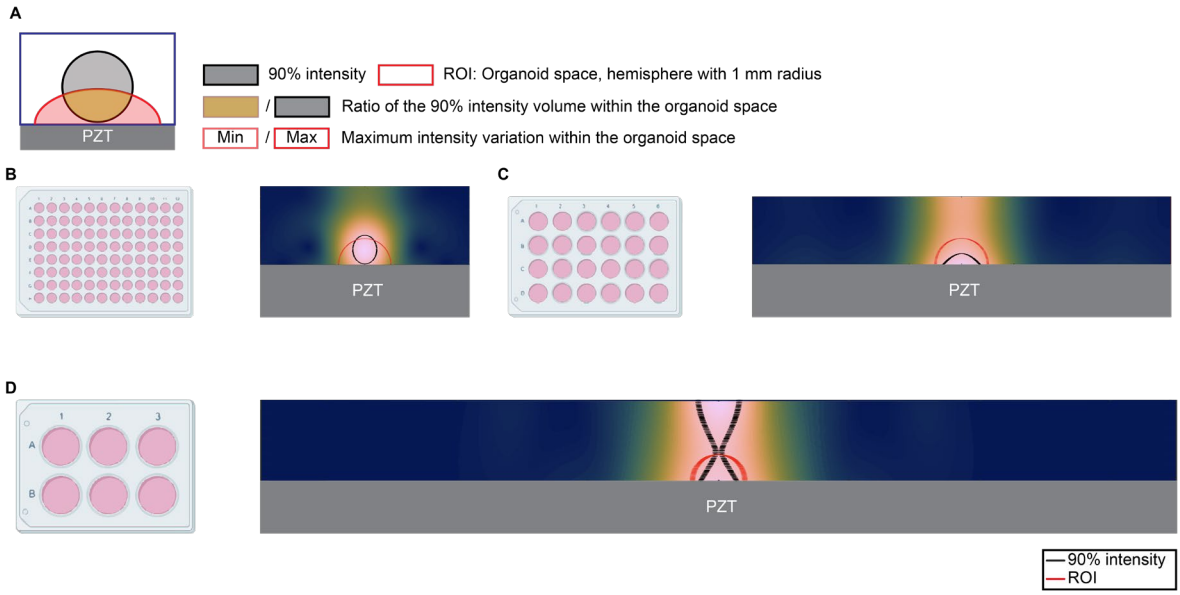

Fig. S2. FEM simulation of the ultrasound beam for optimizing the Well-PZT size. (A) Explanation of borderlines and analytics. (B) Single well simulation results of a 96-well plate. (C) Single well simulation results of a 24-well plate. (D) Single well simulation results of a 6-well plate.

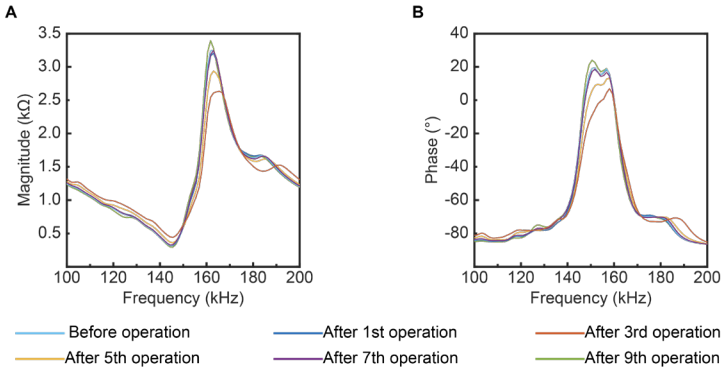

Fig. S3. Robustness test of the platform over 9 operations. (A) Magnitude of measured electrical impedances. (B) Phase of measured electrical impedances.

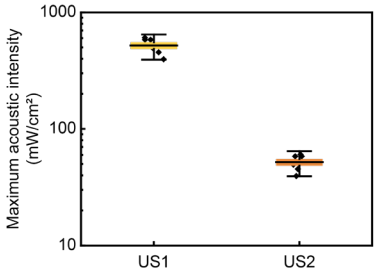

Fig. S4. Evaluation of ultrasound intensity variations across six platforms. Maximum acoustic intensity of each platform for generating US1 and US2.

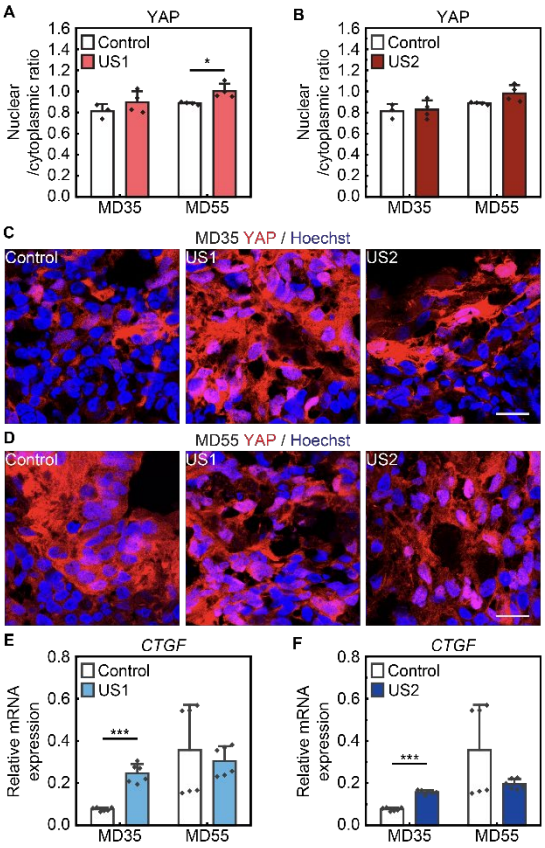

Fig. S5. Additional analysis of ultrasound-induced cellular activation. (**A**) Nuclear translocation ratio of YAP in the US1 group. MD35, two sample two-sided unpaired Student's *t*-test, t=–1.338, p=0.239, n=4. MD55, two sample two-sided unpaired Student's *t*-test, t=–3.245, *p<0.05, n=4. (**B**) Nuclear translocation ratio of YAP in the US2 group. MD35, two sample two-sided unpaired Student's *t*-test, t=–0.260, p=0.805, n=4. MD55, two sample two-sided unpaired Student's *t*-test, t=–2.403, p=0.092, n=4. (**C and D**) Representative immunostaining images of YAP. Scale bar, 20 μm. (**E**) Relative mRNA expression of *CTGF* in the US1 group. MD35, two sample two-sided unpaired Student's *t*-test, t=–9.235, ***p<0.001, n=6. MD55, Mann-Whitney U test, U=18, p=1, n=6. (**F**) Relative mRNA expression of *CTGF* in the US2 group. MD35, two sample two-sided unpaired Student's *t*-test, t=–15.771, ***p<0.001, n=6. MD55, Mann-Whitney U test, U=18, p=1, n=6. Solid bars and error bars indicate mean value and standard deviation, respectively.

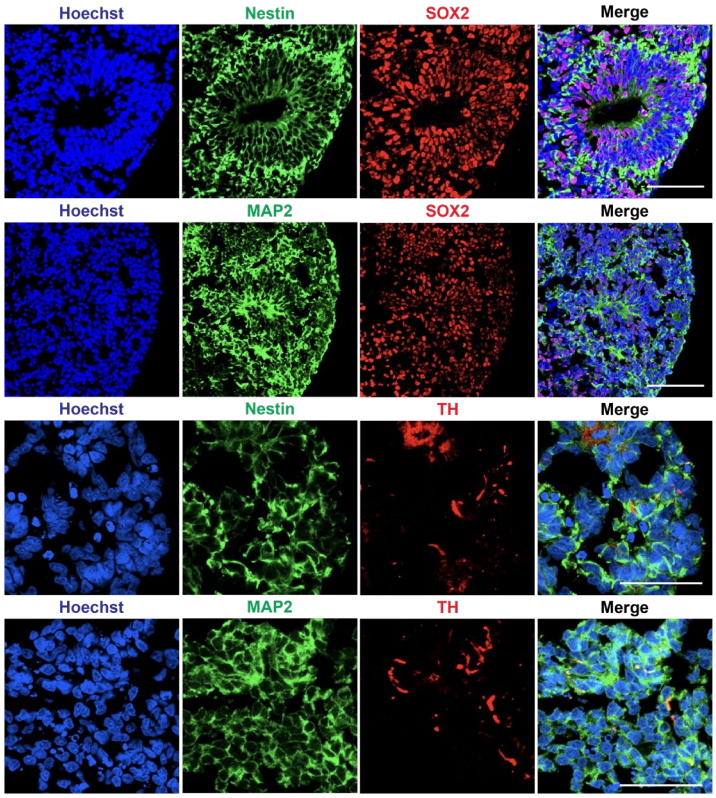

Fig. S6. Characterization of MD1 midbrain organoids. Representative immunofluorescence images demonstrating the expression of neural stem cell marker (Nestin), stemness marker (SOX2), neuron marker (MAP2), and dopaminergic neuron marker (TH). Scale bar, 50 μm

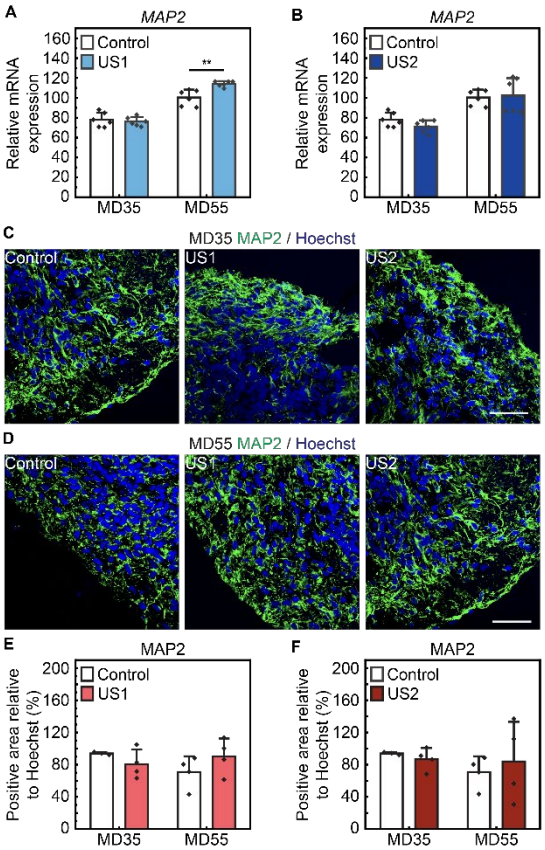

Fig. S7. Effects of ultrasound stimulation on neuronal differentiation. (**A**) Relative mRNA expression of *MAP2* in the US1 group. MD35, two sample two-sided unpaired Student's *t*-test, t=0.519, p=0.617, n=6. MD55, two sample two-sided unpaired Student's *t*-test, t=-3.988, $^{**}p<0.01$, n=6. (**B**) Relative mRNA expression of *MAP2* in the US2 group. MD35, two sample two-sided unpaired Student's *t*-test, t=1.726, p=0.116, n=6. MD55, Mann-Whitney U test, U=18, p=1, n=6. (**C and D**) Representative immunostaining images of MAP2. Scale bar, 50 μm. (**E**) Relative protein level of MAP2 in the US1 group. MD35, two sample two-sided unpaired Student's *t*-test, t=1.452, p=0.240, n=4. MD55, two sample two-sided unpaired Student's *t*-test, t=-1.320, p=0.236, n=4. (**F**) Relative protein level of MAP2 in the US2 group. MD35, two sample two-sided unpaired Student's *t*-test, t=1.017, p=0.381, n=4. MD55, two sample two-sided unpaired Student's *t*-test, t=-0.502, p=0.643, n=4. Solid bars and error bars indicate mean value and standard deviation, respectively.

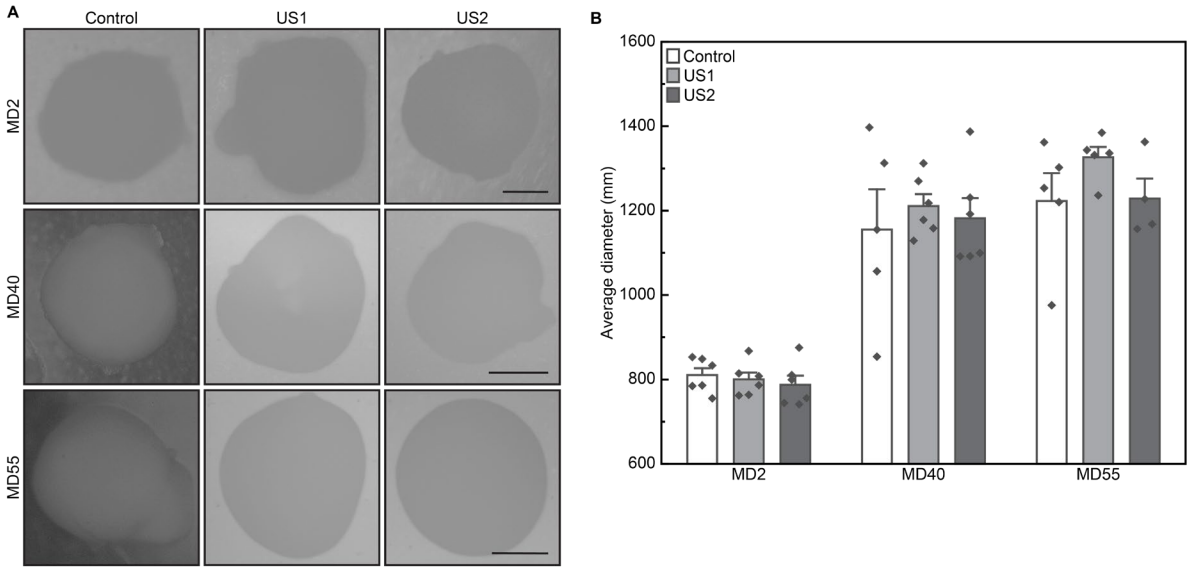

Fig. S8. Effects of ultrasound stimulation on the growth of midbrain organoids. (**A**) Widefield images of midbrain organoids. Scale bar, 250 μm (MD2), 500 μm (MD40), and 500 μm (MD55). (**B**) Size of the midbrain organoids. Solid bars and error bars indicate mean value and standard deviation, respectively.

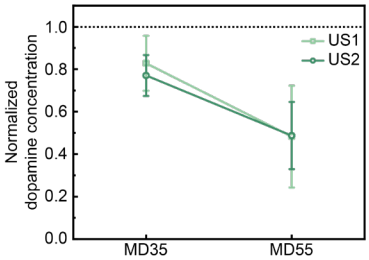

Fig. S9. Analysis of organoid dopamine secretion. Dopamine concentrations were normalized to the control group. US1 group on MD35, one sample Student's *t*-test, t=-2.295, p=0.149, n=3. US2 group on MD35, one sample Student's *t*-test, t=-4.123, p=0.054, n=3. US1 group on MD55, one sample Student's *t*-test, t=-3.739, p=0.065, n=3. US2 group on MD55, one sample Student's *t*-test, t=-5.614, *p<0.05, n=3. Solid bars and error bars indicate mean value and standard deviation, respectively.

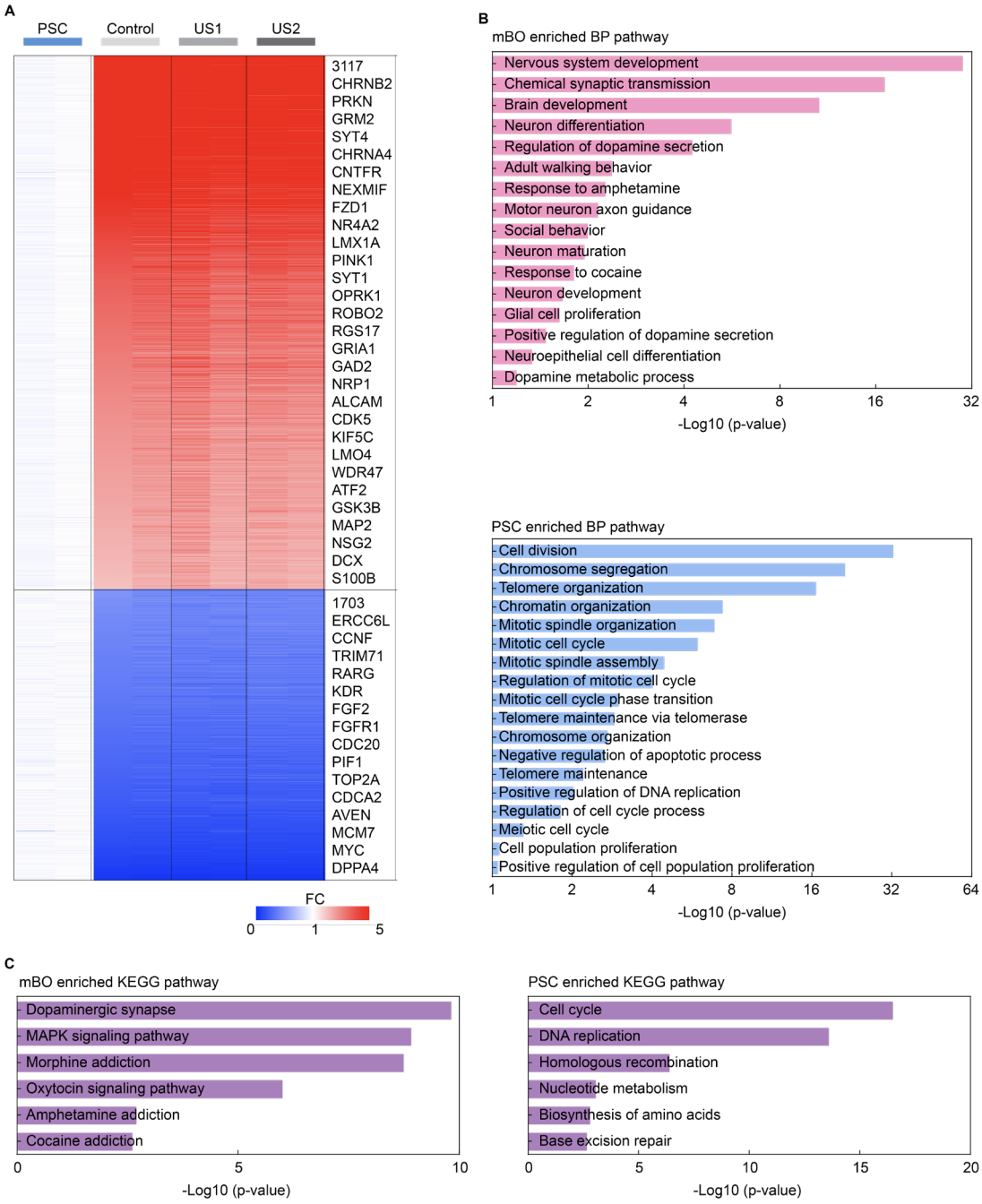

Fig. S10. Total transcriptome analysis of PSCs. (**A**) Heatmap plot for DEGs. (**B**) GO analysis of the PSCs and mBOs. (**C**) KEGG pathway analysis of the mBOs and PSCs.

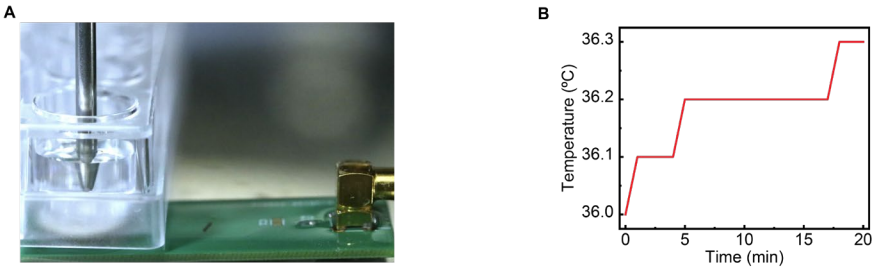

Fig. S11. Measurement of transient temperature changes at the surface of the ultrasound transducer platform. (**A**) Temperature measurement setup in the incubator. (**B**) Temperature measurement results over 20 minutes.

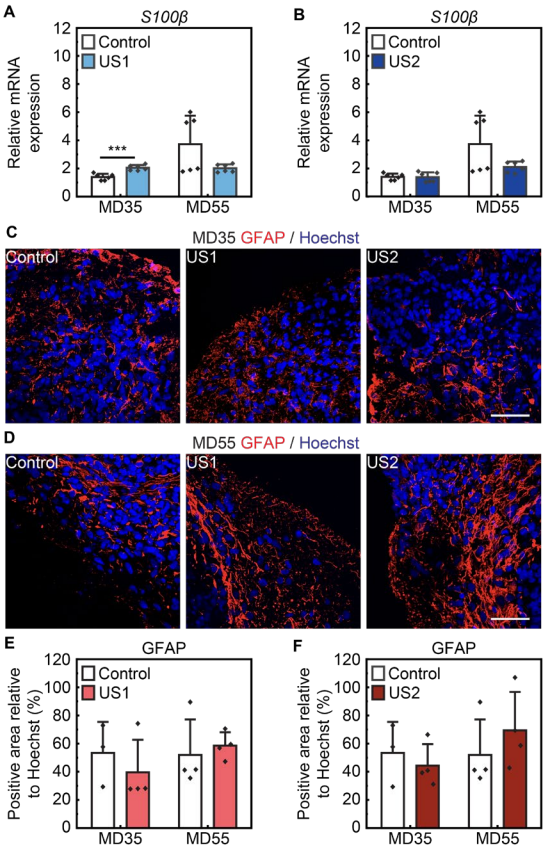

Fig. S12. Effects of ultrasound stimulation on astrocytic differentiation. (**A**) Relative mRNA expression of *S100β* in the US1 group. MD35, two sample two-sided unpaired Student's *t*-test, t=-5.420, ***p<0.001, n=6. MD55, Mann-Whitney U test, U=26, p=0.240, n=6. (**B**) Relative mRNA expression of *S100β* in the US2 group. MD35, two sample two-sided unpaired Student's *t*-test, t=0.152, p=0.884, n=6. MD55, Mann-Whitney U test, U=25, p=0.310, n=6. (**C and D**) Representative immunostaining images of GFAP. Scale bar, 50 μm. (**E**) Relative protein level of GFAP in the US1 group. MD35, Mann-Whitney U test, U=9, p=0.4, n=4. MD55, Mann-Whitney U test, U=4, p=0.343, n=4. (**F**) Relative protein level of GFAP in the US2 group. MD35, two sample two-sided unpaired Student's *t*-test, t=0.599, p=0.587, n=4. MD55, Mann-Whitney U test, U=3, p=0.2, n=4. Solid bars and error bars indicate mean value and standard deviation, respectively.

Data S1. (separate file)

Raw data file for ICC analysis of MD35 organoids

Data S2. (separate file)

Raw data file for ICC analysis of MD55 organoids